

An overview and issues of the sky radiometer technology and SKYNET

Teruyuki Nakajima¹, Monica Campanelli², Huizheng Che³, Victor Estellés^{2,4}, Hitoshi Irie⁵, Sang-Woo Kim⁶, Jhoon Kim⁷, Dong Liu⁸, Tomoaki Nishizawa⁹, Govindan Pandithurai¹⁰,
5 Vijay Kumar Soni¹¹, Boossarasiri Thana¹², Nas-Urt Tugjsurn¹³, Kazuma Aoki¹⁴, Sujung Go^{7,15},
Makiko Hashimoto¹, Akiko Higurashi⁹, Stelios Kazadzis¹⁶, Pradeep Khatri¹⁷, Natalia Kouremeti¹⁶, Rei Kudo¹⁸, Franco Marengo¹⁹, Masahiro Momoi^{5,20}, Shantikumar S. Ningombam²¹, Claire L. Ryder²², Akihiro Uchiyama⁹, Akihiro Yamazaki¹⁸.

- 10 1. Satellite Observation Center, National Institute for Environmental Studies, 16-2 Onogawa, Tsukuba 305-8506, Japan
2. Consiglio Nazionale delle Ricerche, Istituto Scienze dell'Atmosfera e del Clima, via Fosso del Cavaliere, 100, 00133 - Roma, Italy
3. Centre for Atmosphere Watch And Services, CMA Chinese Academy of Meteorological
15 Sciences; 46 Zhong-Guan-Cun S. Ave., Beijing 100081, China
4. Dept. Física de la Terra i Termodinàmica, Universitat de València, Burjassot, Valencia, Spain
5. Center for Environmental Remote Sensing, Chiba University, Chiba 263-8522, Japan
6. School of Earth and Environmental Sciences, Seoul National University, Seoul 08826,
20 Republic of Korea
7. Dept. of Atmospheric Sciences, Yonsei University, Seoul 03722, Republic of Korea
8. Center for Atmospheric Optics, Anhui Institute of Optics and Fine Mechanics, Hefei Institutes of Physical Science, Chinese Academy of Sciences, Hefei, Anhui 230031, China
9. National Institute for Environmental Studies, 16-2 Onogawa, Tsukuba, Ibaraki 305-8506,
25 Japan
10. Indian Institute of Tropical Meteorology, Ministry of Earth Sciences, Pune 411 008, India
11. Environment Monitoring & Research Centre, India Meteorological Department, Ministry of Earth Sciences, Mausam Bhawan, Lodi Road, New Delhi-110003, India
12. Thailand Global Warming Academy, Napamitr Foundation, 234/88 Asoke-Din Daeng
30 Road, Bang Kapi Sub-district, Huai Khwang District, Bangkok 10310, Thailand
13. Physics department, Mongolian University of Science and Technology, 216046, Ulaanbaatar, Mongolia
14. Graduate School of Science and Engineering (Science), University of Toyama, 3190 Gofuku, Toyama 930-8555, Japan

15. Joint Center for Earth Systems Technology (JCET), University of Maryland Baltimore County (UMBC), Baltimore, MD 21228, USA
16. Physikalisch-Meteorologisches Observatorium Davos, World Radiation Center, Dorfstrasse 33, CH-7260 Davos Dorf, Switzerland
- 5 17. Center for Atmospheric and Oceanic Studies, Graduate School of Science, Tohoku University, Sendai, Japan
18. Meteorological Research Institute, Meteorological Agency, Nagamine, Tsukuba 305-0052, Ibaraki, Japan
19. Space Applications and Nowcasting, Met Office, United Kingdom
- 10 20. Graduate School of Science, Tokyo University of Science, Tokyo 162-8601, Japan
21. Indian Institute of Astrophysics, 2nd Block Koramangala, Bangalore 560034, India
22. Department of Meteorology, University of Reading, Reading, RG6 6BB, United Kingdom

15

Abstract

This paper overviews the progress in the sky radiometer technology and development of the network called SKYNET. It is found that the technology has produced useful on-site calibration methods, retrieval algorithms, and data analyses from the sky radiometer observation of aerosol, cloud, water vapor and ozone.

20

A formula was proposed for estimating the accuracy of the sky radiometer calibration constant F_0 using the improved Langley (IL) method, which was found to be a good approximation to observed monthly mean uncertainty in F_0 around 0.5% to 2.4 % at Tokyo and Rome sites and smaller values around 0.3% to 0.5% at the mountain sites of IOA and Davos. A new XIL method was also developed to correct an underestimation by the IL method in case of large aerosol retrieval errors.

25

The RMSD in AOT comparisons with other networks took values less than 0.02 for $\lambda \geq 500\text{nm}$ and a larger value about 0.03 for shorter wavelengths in city areas, and smaller values less than 0.01 in mountain comparisons. Accuracies of Single Scattering Albedo (SSA) and size distribution retrievals are affected by propagation of errors in measurement, calibrations for direct solar and diffuse sky radiation, ground albedo, cloud screening, and version of analysis software called Skyrad pack. SSA values from SKYNET were up to 0.07 larger than those from AERONET, and major error sources were identified as underestimation of SVA and cloud contamination. Correction of these known error factors reduced the SSA difference to less than 0.03.

30

Retrievals of other atmospheric constituents by the sky radiometer were also reviewed. Retrieval accuracies were found to be about 0.2 cm for precipitable water vapor amount and 13 Dobson Unit for column ozone amount. Retrieved cloud optical properties still showed large deviations from validation data, suggesting need to study causes of differences.

5 It is important that these recent studies on improvements presented in the present paper are introduced in the existing operational systems and future system of the International Skynet Data Center.

1. Introduction

10 A sun–sky radiometer is a narrow band filter photometer able to perform measurements of direct solar and diffuse sky radiation at selected wavelengths and at several scattering angles. Observed data have large information contents for aerosol, cloud, and gaseous constituents, but are difficult to retrieve because of the need for full radiative transfer computation to quantify single and multiple scattered radiation.

15 The origin of the idea of the technology dates back to the beginning of the last century (Shaw, 2006). Long-term direct solar and diffuse sky measurements were carried out during 1923-1957 by the Smithsonian Astronomical Observatory by monitoring the solar constant with a pyrheliometer at Montezuma (Chile) and Table Mountain (California) (Abbot, 1911; Ångström, 1961, 1974; Roosen et al., 1973; Hoyt, 1979a, b). Diffuse sky irradiance in the circumsolar or
20 solar aureole region was measured by the pyranometer to correct for the atmospheric effects in the measured solar constant (Abbot and Aldrich, 1916). This method was also used by Kalitin et al. (1930), Fesenkov (1933), and Pyaskovskaya-Fesenkova (1957) (Terez and Terez, 2003). By 1970s, spectral measurements of the direct solar radiation became popular for air pollution monitoring by introduction of a low cost compact narrow band radiometer called a
25 sunphotometer with a silicon photodiode and cutoff or interference optical filters (Volz, 1959, 1974). In parallel, pioneering measurements of the spectral diffuse sky radiance started from ground and aircraft (Bullrich, 1964; Bullrich et al., 1967, 1968; Murai, 1967; Eiden, 1968; Green et al., 1971; Gorodetskiy et al., 1976; Twitty et al., 1976). They were attracted by the characteristic radiance distributions including bright circumsolar region and neutral points of
30 the degree of polarization in the sky dome. Theoretical and inversion schemes for the involved ill-conditional problems were studied for data analysis (Deirmendjian, D., 1957, 1959; Phillips, 1962; Twomey 1963; de Bary, 1964; Turchin and Nozik, 1969; Yamamoto and Tanaka, 1969; Dave, 1971; Shifrin et al., 1972; Shifrin and Gashko, 1974).

35 By 1980s, analyses of combined sun and sky radiation data became comprehensive (e.g., O'Neill and Miller, 1984a, b; Tanaka et al., 1986; Tanré et al., 1988) after the full yet fast

radiative transfer computation became possible, allowing quantification of the multiple scattering component of sky radiance and retrieval of the column-averaged size distribution and the complex refractive index of polydispersed aerosol (Twitty, 1975; Weinman et al., 1975; Box and Deepak, 1978, 1979; Nakajima et al., 1983; O'Neill and Miller, 1984b; Tanré et al., 5 1988; Tonna et al., 1995; Dubovik and King, 2000; Dubovik et al., 2000, 2002). Networks of the radiometer have been developed to utilize sun and sky measurement data for various applications such as satellite remote sensing validation, air pollution monitoring and study of climate effects of atmospheric constituents, as overviewed by Holben et al. (2001). The largest network is the NASA AERONET (Holben et al., 1998) developed in the early 1990s and 10 currently with more than 500 radiometers named the sun-sky photometer. Later in around the 2000s, SKYNET was formed with the sky radiometer (Nakajima et al., 2007). Compared to the AERONET technology, SKYNET has several differences in measurement and analysis methods.

The SKYNET is for research purposes without a centralized data analysis system and 15 information is scattered in independent papers and documents, which makes SKYNET difficult to understood by the science community. In this situation this paper intends to make an overview of key findings and issues of the SKYNET providing better information for the community.

20 **2. Sun and sky measurements by the sky radiometer**

The SKYNET is a research group of users of the sky radiometer initiated around the time of the East Asian Regional Experiment (EAREX) 2005 (Nakajima et al., 2007), one of the regional experiments under the UNEP Atmospheric Brown Cloud (ABC) project (Ramanathan et al., 2007). A number of sky radiometers were deployed in the East Asian region for 25 measuring the aerosol optical properties in order to estimate the aerosol impact on the earth's radiation budget (Takamura et al., 2004; Khatri et al., 2010). Since then, users of the sky radiometer have kept growing globally and the number of sky radiometers now exceeds 100 units. Table 1 and Fig. 1 show the sky radiometer sites as recognized by the International Skynet Committee (ISC). Users established regional sub-network groups in China, Europe, 30 India, Japan, Korea, Mongolia, and South East Asia for data analysis and formed the ISC to discuss international collaboration issues (Fig.2). Historically two major groups were grown for regional data collection and analysis: the SR-Center for Environmental Remote Sensing (SR-CEReS) of Chiba University (Takamura et al., 2004, 2009, 2013) and the European Skynet Radiometers network (ESR) (Campanelli et al, 2004, 2007, 2012). Analysis systems were 35 developed by the sub-networks independently, so that analysis methods and data archive

systems have not been unified. Table 2 lists the archived geophysical parameters, versions of the retrieval software called Skyrad pack, and data availability in the known data archives. The table indicates the features of archives are different from each other and difficult for use by the science community.

5 In 2017, the SKYNET has become a contributing network of the WMO Global Atmospheric Watch (GAW) (<https://community.wmo.int/activity-areas/gaw>). In this expanding situation of SKYNET with more burden and responsibility, the ISC decided to establish the International SKYNET Data Center (ISDC) at the National Institutes for Environmental Studies (NIES) in Japan to start a shared data collection and analysis based on the MOU between users and the
10 ISDC. Among the sites in Table 1, the ISDC started receiving data from 25 sites in the world. The ISDC is going to provide standard products from the SKYNET network, whereas the regional sub-networks will develop new research products and test new methodologies.

The main instrument of the SKYNET is the sky radiometer manufactured by PREDE Co. Ltd. Several versions of the radiometer have been made by users' requests. POM-01 is the
15 standard version with seven wavelengths of $\lambda = 315, 400, 500, 675, 870, 940$ and 1020 nm and POM-02 is an extended version with UV wavelengths of 340 nm and 380 nm, and shortwave infrared wavelengths of 1600 nm and 2200 nm. Channels of 315 nm and 940 nm are installed for ozone and water vapor amount retrievals. Full-widths at half-maximum of band-pass filters are
20 longer wavelengths. There is a modified version of POM-02 for lunar photometry (Uchiyama et al., 2019). Shipborne versions have been also built (Kobayashi and Shiobara, 2015).

Sky radiometer readings of direct solar and diffuse sky measurements, V_d and V_s , are related to the direct solar irradiance F_d and sky radiance \bar{L}_s at the mean earth's orbit as,

$$F_d = C_R R_{es}^2 V_d, \quad \bar{L}_s = \frac{F_s}{\Delta\Omega} = C_R \frac{R_{es}^2 V_s}{\Delta\Omega}, \quad (1)$$

25 where C_R is the radiometric sensitivity or calibration coefficient of the radiometer to translate the radiometer reading to irradiance unit, say $\text{Wm}^{-2} \text{nm}^{-1}$; $\Delta\Omega$ is the Solid Viewing Angle (SVA) of the radiometer; R_{es} is the sun-earth distance in the astronomical unit. SKYNET remote sensing uses the beam transmittance T_d of the atmosphere and relative sky radiance R (Nakajima et al., 1986) defined as,

$$30 \quad T_d \equiv \frac{F_d}{F_0} = \exp(-m_0 \tau), \quad (2a)$$

$$\tau = \tau_a + \tau_m, \quad \omega\tau = \omega_a \tau_a + \omega_m \tau_m, \quad (2b)$$

$$R(\theta, \phi; \theta_0, \phi_0) \equiv \frac{\bar{L}_s(\theta, \phi; \theta_0, \phi_0) / m}{F_d} = \frac{1}{m \Delta\Omega} \frac{V_s}{V_d}, \quad (2c)$$

where τ is the Optical Thickness (OT) of the atmosphere consisting of molecular optical thickness τ_m and Single Scattering Albedo (SSA) ω_m , and Aerosol Optical Thickness (AOT) τ_a and SSA ω_a in the clear sky condition; F_0 is the Extraterrestrial Solar Irradiance (ESI); (θ_0, ϕ_0) and (θ, ϕ) are zenith and azimuthal angles of the sun and the line of sight of the sky radiometer, respectively; m_0 and m are optical airmasses for solar insolation and line of sight of the radiometer, which are approximated as $1/\cos(\theta_0)$ and $1/\cos(\theta)$ for plane-parallel geometry of the atmosphere. SKYNET adopts on-site calibration routines to determine the two radiometric constants, F_0 and $\Delta\Omega$, by the Improved Langley plot method (hereafter, IL or ILP) and the disk scan method (Nakajima et al, 1996; Boi et al., 1999; Uchiyama et al., 2019a, b) as discussed in Sections 3 and 4. Under the condition that C_R and F_0 do not change between time of measurement and time of F_0 determination, T_d and R do not depend on the calibration coefficient C_R , so that we can select the radiometer reading for F_0 , i.e. $C_R=1$, without the absolute radiometric calibration. On this assumption, F_0 in the radiometer reading is sometimes called a calibration constant. In order to meet this condition, therefore, the on-site calibration is required to be performed as frequent as possible to monitor change of C_R due to machine condition change and F_0 change due to solar luminosity change.

Standard measurement protocols of SKYNET are as follows. Direct solar irradiance is measured every 1 minute. Diffuse sky radiance is measured by full almucantar scan at scattering angles from set of $\Theta = \{2^\circ (1^\circ) 5^\circ, 7^\circ, 10^\circ (5^\circ) 30^\circ (10^\circ) 160^\circ\}$ for $\theta_0 \leq 78^\circ$, whereas the forward almucantar scan is made in $\Theta \leq 30^\circ$ for $\theta_0 > 78^\circ$. The sky radiometer has several angle scan modes, i.e. almucantar scan, principal plane scan, cloud scan, and solar disk scan. There are two temporal sampling modes of regular time interval of 10 minutes (mode-1) and regular solar air mass interval of 0.25 (mode-2). Most of the sites in Table 1 adopt the mode-1 measurement with one-side almucantar scan. The disk scan mode is scheduled once a week at 10:00am local time, though the scan time can be changed by the user's plan. A cloud scan mode at nadir is taken every 10 minutes at POM-02 sites and some POM-01 sites.

Once the radiometric constants are determined, the direct solar irradiance F and relative sky radiance R are used for the Level-2 (L2) analysis, i.e., retrievals of the geophysical parameters of aerosol, cloud, water vapor and ozone as discussed later in Section 5. The flow of sky radiometer measurements and data analysis are schematically depicted in Fig. 3. As overviewed in the following sections, F_0 and SVA are obtained on site through various Langley plot methods and solar disk scan method using data from direct solar and forward scan measurements. Cloud screening is also performed differently by sub-networks. The ESR performs a cloud screening for a direct solar measurement at 1 min frequency by a procedure based on the methodology developed by Smirnov et al. (2000) (Estellés et al., 2012a; Song et al.,

2014). Cloud screening for sky measurements uses the downward shortwave radiative flux measured by a co-located pyranometer (Khatri and Takamura, 2009), otherwise they do not perform cloud screening for sky data. CEReS conducts the cloud screening with the method of Khatri and Takamura (2009), but without using global irradiance data from a pyranometer (Irie et al., 2019). It corresponds to the combination of a spectral variability test (Kaufman et al., 2006) and statistical analysis test of Smirnov et al. (2000) including checking the number of data, a diurnal stability check, smoothness criteria, and three standard deviation criteria, but without triplet stability criteria test. We do not use several QC tests such as the angular steepness of the solar aureole for a stricter cloud filter as in AERONET (Giles et al., 2019).

10 To obtain data for L2 data analysis for retrieval of geophysical parameters for atmospheric constituents, an analysis software called Skyrad pack has been developed (Nakajima et al., 1996; Hashimoto et al., 2012) and publicly opened on the OpenCLASTR shareware site (http://157.82.240.167/~clastr/data_policy.html) for the research community. Various L2 products are retrieved by the Skyrad pack such as spectra of AOT, its slope called Ångström exponent (AE), Size Distribution Function (SDF), SSA, Complex Refractive Index (CRI), asphericity, cloud optical thickness (COT), cloud effective particle radius (CER), and water/ice phase from data in the non-gas absorbing channels, Precipitable Water Vapor (PWV) and column ozone amount (O₃) from the gas absorbing channels, as explained in the following sections. Common operational products by the sub-networks are AOT, AE, SDF, SSA, and CRI assuming Mie particles. Other products have been retrieved by research studies. The current operating versions are version 4.2 and 5, and a version of Meteorological Research Institute of Japan Meteorological Agency (MRI version) developed by Kobayashi et al. (2006, 2010).

3. Radiometric calibration of the direct solar irradiance measurements

25 In the case of non-gas absorption channels, the Standard Langley plot method (SL or SL plot method) can be used to obtain F_0 by plotting the logarithm of the Lambert-Beer's law Eq. (2a) versus m_0 ,

$$\ln F_d = \ln F_0 - m_0 \tau, \quad (3)$$

to extrapolate the linear regression line to $m_0=0$. It is known, however, that an air mass dependence or a quadratic time dependence of AOT introduces a serious error in the SL as claimed by Shaw (1976). Correction methods to this problem were proposed by O'Neill and Miller (1984a, b) and Tanaka et al. (1986) with use of a time dependence of the circumsolar radiance of which the major part is approximated by the single scattered radiance proportional to the OT along the solar almucantar circle ($\theta = \theta_0$), given as,

$$R(\theta, \phi; \theta_0, \phi_0) = \omega\tau P(\Theta) + R_{mult}(\theta, \phi; \theta_0, \phi_0), \quad (4)$$

where P is the normalized scattering phase function at the scattering angle of Θ and R_{mult} is the multiple scattered radiation. Tanaka et al. (1986) used a forward scattering around $\Theta = 20^\circ$ at which the phase function is relatively independent of the SDF of the atmospheric particulate matter. Extending this principle, SKYNET adopts the IL method to extrapolate Eq. (3) regarding the total scattering optical path,

$$x = m_0 \omega \tau, \quad (5a)$$

or its aerosol part,

$$x_a = m_0 \omega_a \tau_a, \quad (5b)$$

which can be retrieved from the forward scattering part, $\Theta \leq 30^\circ$, of the relative sky radiance R , Eq.(4). The formulae in Eqs. (4) and (5) indicate that x_a is relatively accurately retrieved from the inversion of the forward scattering part of the sky radiance. We use Eq. (5b) in most of ILP by sub-networks.

The accuracy of F_0 estimation by the IL method depends on the turbidity condition of the site.

The theory of a linear regression model is formulated with a normal random observation error u as,

$$y_i = a + bx_i + u_i, \quad i = 1, \dots, n, \quad (6a)$$

$$a = \ln F_0, \quad x = m_0 \omega \tau, \quad y = \ln(F), \quad (6b)$$

where n is the number of observations. Here, we omit subscript "a" from τ_a and ω_a for the sake of compact notation unless otherwise specified. Equation (6) gives estimates of regression coefficients and their dispersion as,

$$b = \frac{\langle (x - \bar{x})(y - \bar{y}) \rangle}{\sigma_x^2}, \quad a = \bar{y} - b\bar{x}, \quad (7a)$$

$$\sigma_b^2 = \frac{\varepsilon_u^2}{n\sigma_x^2}, \quad \sigma_a^2 = \frac{\varepsilon_u^2}{n} \left(1 + \frac{\bar{x}^2}{\sigma_x^2}\right), \quad (7b)$$

where upper bar and $\langle \rangle$ stand for averaging operation and ε_u is the root mean square error (RMSE) for u . The standard linear regression theory assumes x is an independent variable to be related to a dependent variable y which includes random residual of the fitting u . Based on this assumption, the dispersion of x is given as,

$$\left(\frac{\sigma_x}{\bar{x}}\right)^2 \sim \frac{\sigma_{m_0}^2}{\bar{m}_0^2} + \frac{\sigma_\tau^2}{\bar{\tau}^2} + \frac{\sigma_\omega^2}{\bar{\omega}^2}, \quad (8a)$$

where $\sigma_{m_0}^2$, σ_τ^2 and σ_ω^2 are dispersions of sampling airmasses $\{m_{0i}\}$, natural variations in $\{\tau\}$ and $\{\omega\}$ during the ILP, respectively. The dispersion of residual $\{u_i\}$ is approximated by the

sum of mean square errors of τ and ω , i.e. ε_τ^2 and ε_ω^2 , caused by the inversion process of Eq.

(4) as,

$$\varepsilon_u^2 = b^2 \bar{m}_0^2 [(\bar{\omega} \varepsilon_\tau)^2 + (\bar{\tau} \varepsilon_\omega)^2] + \varepsilon_F^2, \quad (8b)$$

where ε_F^2 is the mean square error of $\{y_i\}$ caused by observation by the radiometer, which is usually small and neglected from the formula. The budget of dispersions Eq. (8a) leads to the following estimate for a typical air mass sampling from $m_1=1.3$ to $m_2=3.5$ and atmospheric conditions of large optical parameter change from $\tau_1=0.2$ to $\tau_2=0.4$, and from $\omega_1=0.85$ to $\omega_2=0.95$ during the ILP as,

$$\left(\frac{\sigma_x}{\bar{x}}\right)^2 \approx \frac{1}{3} \left(\frac{m_2 - m_1}{m_2 + m_1}\right)^2 + \frac{1}{3} \left(\frac{\tau_2 - \tau_1}{\tau_2 + \tau_1}\right)^2 + \frac{1}{3} \left(\frac{\omega_2 - \omega_1}{\omega_2 + \omega_1}\right)^2 = 0.070 + 0.037 + 0.001, \quad (9)$$

if we assume a regular sampling of linear change models for m , τ , and ω . This budget indicates that the wide sampling of air mass is the main contributor to decrease σ_a^2 . The IL method allows selection of the atmospheric condition in which τ and ω undergo natural variations that help to increase σ_x and thus decrease σ_a . But such selection of unstable atmospheric conditions may increase inversion errors, ε_τ and ε_ω , wasting the benefit of natural changes in ω and τ . It is also possible to have a change in the atmospheric conditions during a short time of less than 5 min in one full angle scan, causing unexpected errors. Sub-networks, therefore, have their own screening protocols for ILP using stability of time sequence of variables to reject ill condition data for ILP. They also reject large AOT cases to secure the calibration accuracy, e.g. AOT > 0.4 by ESR (Campanelli et al., 2004).

Combining Eqs. (7) and (8), we have the following estimate for σ_a assuming b and ω are close to 1,

$$\sigma_{a,IL} = \frac{3.5}{\sqrt{n}} \frac{\bar{m}_0^2}{|m_2 - m_1|} \gamma \bar{\tau} \sim \frac{9.2}{\sqrt{n}} \gamma \bar{\tau} \sim \frac{1.3}{\sqrt{n}} \bar{\tau}, \quad (10a)$$

$$\gamma \equiv \sqrt{\left(\frac{\varepsilon_\tau}{\bar{\tau}}\right)^2 + \left(\frac{\varepsilon_\omega}{\bar{\omega}}\right)^2}. \quad (10b)$$

The third expression of rhs Eq. (10a) is an estimate for $m_1=1.3$ and $m_2=3.5$ and the rightmost one is an approximation with 10% relative errors in inversion of τ and ω as a typical example of ILP. This estimate indicates the accuracy of $\ln(F_0)$ from the IL method is proportional to the OT during ILP operation at the site. Table 3 lists mean values of n , τ_a and $\sigma_{a,IL}$ per 30 days (month) obtained by ILP operation carried out at Tokyo University of Science (TUS) and Rome sites.

The table shows the monthly value of $\sigma_{a,IL}$ ranges from 0.5% to 2.4% with a tendency to increase with decreasing wavelength. We also estimated $\sigma_{a,IL}$ by Eq. (10) with optimum

γ -values of 7% and 15% for Tokyo and Rome, respectively. These estimates correspond to 5% and 11% for relative retrieval errors $\varepsilon_{\tau}/\langle\tau\rangle$ and $\varepsilon_{\omega}/\langle\omega\rangle$ during ILP operation.

The monitoring ability of F_0 by IL on site has merits such as low cost, frequent calibration to detect the changing constants and a short-term ESI change, and minimizes the radiometer environmental change avoiding shipping for calibration. The error in F_0 is propagated to cause an error in OT from Eq. (3) as,

$$\varepsilon_{direct,\tau} \sim \frac{\sigma_a}{m_0}. \quad (11)$$

A rough estimate of AOT error by the IL calibration is expected to be the order of 0.003 to 0.01 for $m_0=2$ in the case of Table 3, though real errors depend on detailed setup and observation sequence at each site. It is important to compare this accuracy of IL with that of SL. In the SL case, we assume $x=m$ in Eq. (6a), so that the error estimate Eq. (7b) is reduced to the following expression as,

$$\sigma_{a,SL}^2 = \frac{\tau'^2}{n} \left(1 + \frac{\bar{m}^2}{\sigma_m^2}\right), \quad (12a)$$

where we assume the error in a is caused by a part of OT change during the SL plot which tends to the inverse of the optical airmass as,

$$\tau = \bar{\tau} + \frac{\tau'}{m}. \quad (12b)$$

A measure of OT change during airmass change from m_1 to m_2 can be defined as

$$\delta_{\tau} \equiv \frac{\tau_1 - \tau_2}{2} = \frac{1}{2} \left(\frac{1}{m_2} - \frac{1}{m_1} \right) \tau' = 0.24\tau'. \quad (12c)$$

The rightmost estimate is given for $m_1=1.3$ and $m_2=2.5$ as an example. If we assume $\delta_{\tau} / \bar{\tau} = 0.1$ as same as inversion error in the estimate of IL accuracy, the following estimate is given as,

$$\sigma_{a,SL} = \frac{1.6}{\sqrt{n}} \bar{\tau}. \quad (13)$$

This estimate of the SL error is similar to that of IL given in Eq. (10), suggesting the SL performance is similar to or slightly larger than that of IL under conditions of 10% change in OT during the SL plot. Selection of the calibration methods, therefore, depends on the character of the turbidity conditions at the site. There are reports from city-area sites, such as Rome, Beijing and Chiba city, that the accuracy of SL method exceeds 1 to 2% worse than that of IL method, suggesting $\varepsilon_{\tau} / \bar{\tau} > 0.1$ commonly happens at these sites, so that we recommend comparison of F_0 values from both SL and IL methods to diagnose the calibration quality of the SL and IL methods. At the same time, we recommend high mountain calibration and/or transfer

of calibration constants from a well-calibrated standard radiometer to keep the on-site IL calibration healthy.

The SKYNET community performed high mountain calibrations at Mauna Loa (USA, 3397mMSL) and two similar pristine aged-background sites (AOT₅₀₀~ 0.05, AOT at $\lambda=$ 500nm), Indian Astronomical Observatory (IAO), Hanle (Mt. Saraswati, 32°47'N, 78°58'E, 4500m MSL) and Merak (33°48'N, 78°37'E, 4310m MSL), located in the high-altitude Ladakh region in the north-western Himalaya. Figure 4 shows retrieved values of F_0 and SVA from the observation taken by a single instrument (POM-01) from IAO-Hanle during January 2008-December 2010 and June 2015-December 2018 and Merak during January 2011-May 2015. They used the Skyrad pack software for data screening with a condition of RMSD of SVAs below 0.20, while the median value of the long-term data as much as 0.05. The observation were taken from a wide range of AOTs with minimum (instantaneous) 0.01 to maximum 0.22 with the annual averaged AOT as 0.045 ± 0.026 at 500 nm during 2008 to 2018 at the two sites. Due to limiting cloudy conditions in the afternoon, 35% of the disk scanning work is performed in between 8-9am at this site. Since the disk scanning procedure takes around 20-25 minutes to complete the entire wavelengths, it is apparent that in some cases, some wavelengths may have been affected by thin (cirrus) clouds which carried by strong winds (above 15 m/s) at both the sites. The figure indicates the RMSD of $\ln(F_0)$ from SL and IL methods agree within about 0.5%. This F_0 uncertainty is smaller than the minimum value of $\sigma(a,IL)$ about 0.5% at Tokyo and Rome shown in Table 3 and corresponds to an estimate Eqs. (10) and (13) assuming the mean AOT at the site of order of 0.03 at $\lambda= 500\text{nm}$ and $n= 100$. The figure shows that the disk scan method, discussed in the next section, was obtained with monthly mean SVA within 1.5% for all the spectral channels. The disk scan was performed from observations taken under full clear sky conditions with minimum 3-5 days data in every month (Ningombam et al., 2014). Therefore, there are 12 values of SVA in all the spectral channels in a year. The vertical bar indicates a representative RMSD of monthly means in each year.

The first QUALity and TRaceability of Atmospheric aerosol Measurements (QUATRAM, <http://www.euroskyrad.net/quatram.html>) Campaign compared the F_0 -value from IL method with that of the standard Precision Filter Radiometer (PFR) (Kazadzis et al., 2018b) of the World optical depth Research and Calibration Center (PMOD/WRC). A preliminary analysis showed the difference is 0.3% at Davos (1590m MSL) where the mean AOT₅₀₀ is 0.15 and AOT₅₀₀ in clean aerosol conditions is 0.05. This F_0 uncertainty is similar to those of the IOA sites and again smaller than the minimum value in Table 3, indicating the importance of the careful constant calibration effort at high mountains.

Another important point to note is that comparison of Eqs. (3) and (6) lead to the following relation,

$$b = -\frac{1}{\omega}. \quad (14)$$

The forward scattering analysis of the IL method prescribes the refractive index, so that it is highly possible for x in Eq. (5a) to include a factor type systematic error like,

$$x = Cx_0. \quad (15a)$$

In this case, Eq. (6) results in the following relation between fitted and true values of a and b , a_0 and b_0 , as

$$b = \frac{1}{C}b_0, \quad a = \bar{y} - \frac{1}{C}b_0C\bar{x}_0 = \bar{y} - b_0\bar{x}_0. \quad (15b)$$

This result shows that the formula of a in Eq. (7a) is invariant to the factor type error indicating the robustness of the IL calibration. On the other hand, the b -value changes depending on the value of C and takes a value $-1/\omega$ according to Eq. (14). Boi et al. (1999) utilized this point and proposed an iterative IL method to improve the F_0 -value and find the optimum CRI by trying several refractive indices. They reported the method can improve the precision of F_0 by 30%, e.g. 2% to 1.5%.

There is another caution regarding use of the formulae Eq. (7a). In the real observation, it is difficult to separate natural variations and inversion errors of τ and ω , so that the dispersion σ_x tends to include undesired inversion errors, that lead the IL method to underestimation of a and b as understood by Eq. (7b). We are testing a new solution to this problem, named the cross IL method (XIL), which exchanges the role of x and y in the regression analysis, i.e.,

$$x_i = \alpha + \beta y_i + v_i, \quad i = 1, \dots, n, \quad (16a)$$

$$b = \frac{1}{\beta}, \quad a = -\frac{\alpha}{\beta}. \quad (16b)$$

Figure 5 presents retrieved values of a ($=\ln F_0$) from IL and XIL methods with ten ensemble runs of an idealized experiment with $F_0=1$, $\omega=1$, $\tau=0.1$; $n=20$ and $m=1.3$ to 3.5 as a function of normal random errors ε_x in x . The figure shows that the IL method underestimates the a -value, while the XIL stays accurate within RMSE less than 0.03 up to $\varepsilon_x=0.01$ (10% of $\tau=0.1$) and 0.05 at $\varepsilon_x=0.025$ (25% of $\tau=0.1$), as consistent with Eq. (10). Figure 6 and Table 4 compares results of IL and XIL methods with the following screening conditions applied to 38 sets of real Langley plot data at TUS site for four months from February through May 2017:

$$m_2/m_1 \geq 2, \quad b(\text{SL}) < 10, \quad 0.8 \leq b(\text{IL}), \quad \text{and} \quad b(\text{XIL}) \leq 1.2, \quad \varepsilon_u(\text{IL}), \quad \text{and} \quad \varepsilon_u(\text{XIL}) \leq \varepsilon_{u0}, \quad (17)$$

where m_1 and m_2 are lower and upper limits of airmass in the ILP. The threshold residual ε_{i0} is given as 0.02, 0.03 and 0.05. The figure and table indicate that the a -value from SL is largely scattered, suggesting determination of F_0 by SL at turbid sites like Tokyo is not recommendable. On the other hand, a -values from IL and XIL converge on a regression line within differences of 2-3%, with a tendency of systematically smaller values by IL than those from XIL method by amounts of ε_{i0} and $\varepsilon_{i0}/2$, respectively. Although the difference between IL and XIL is not large as far as we select low noise data, we would like to recommend the XIL method to be applied to 5 to 10 Langley plot data sets in order to secure the accuracy of 1% to 2% in F_0 using the screening conditions of Eq. (17). The figure also shows that we can detect a long-term decreasing trend of a -value by about 10% during the period at the TUS site.

4. Sky radiance calibration for the sky radiometer

Several methods have been proposed for on-site calibration of the sky radiance measured by the sky radiometer, such as solar disk scan method, point-source method or lamp scan method, and diffuse plate method (Nakajima et al., 1986, 1996; Boi et al., 1999). Among them, the solar disk scan method has been routinely used in the SKYNET measurement of the SVA of the sky radiometer by scanning a circumsolar domain (CSD) of $\pm 1^\circ$ by $\pm 1^\circ$ around the sun with every 0.1° interval.

The irradiance received by the radiometer, which is aimed at the direction (x, y) in a Cartesian coordinate system of angular distance from the center of the solar disk at origin $(x=0, y=0)$, is an angular integration of radiances weighted by the response function of the radiometer f_R in the field of view (FOV),

$$F(x, y) = \iint_{FOV} dx' dy' f_R(x' - x, y' - y) L(x', y'). \quad (18)$$

In the case of diffuse sky radiance measurement, the SVA of the radiometer is given from Eqs. (1) and (18) as,

$$\Delta\Omega = \iint_{FOV} dx' dy' f_R(x', y'). \quad (19)$$

In the case of the solar disk scan, the main term for F is given as follows under conditions of small contribution from diffuse sky radiation in the CSD,

$$F(x, y) = \iint_{FOV} dx' dy' f_R(x' - x, y' - y) L_d(x', y'), \quad (20a)$$

where L_d is the radiance distribution of the solar disk. The angular aperture of the sky radiometer is about 1° , whereas the solar disk radius is about 0.5° , so that we can measure the solar disk-averaged value of the radiometer response function as,

$$\bar{f}_R(x, y) = \frac{F(x, y)}{F_d}. \quad (20b)$$

From Eqs. (1), (20a) and (20b), the following normalization condition has to be fulfilled,

$$\bar{f}_R(0, 0) = 1. \quad (20c)$$

The SVA can be obtained by the angular integration of the radiance in the CSD as,

$$\begin{aligned} I &\equiv \iint_{CSD} dx dy \bar{f}_R(x, y) = \frac{1}{F_d} \iint_{CSD} dx dy \iint_{FOV} dx' dy' f_R(x' - x, y' - y) L_d(x', y') \\ &= \frac{1}{F_d} \iint_{FOV} dx' dy' L_d(x', y') \iint_{CSD} dx dy f_R(x' - x, y' - y) = \Delta\Omega \end{aligned} \quad (20d)$$

The last expression is obtained by Eqs. (19) and (20c), if the size of CSD is large enough to include FOV or the contribution outside the CSD is small. These equations indicate flatness of the response function around the optical axis should be secured in manufacturing the sky radiometer for stable measurement of the direct solar radiation through Eq. (20b). The perfect flatness is realized by optics without an objective lens, which is useful for moving platform such as aircraft and ship (Nakajima et al., 1986).

Analyzing data from the solar disk scan, Uchiyama et al., (2018b) found an underestimation of SVA from the disk scan method of 0.5 % to 1.9 % and proposed a correction method by extending CSD size up to scattering angle of 2.5° assuming an extrapolation function as illustrated in Fig. 7. They also discussed that the SVA error by the disk scan can exceed 1% for large AOT conditions such as AOT550 > 0.5 and proposed a subtraction method using sky radiance calculated from the size distribution retrieved from the relative radiance. This subtraction method can reduce the error to 0.5% for AOT550 < 2 for sky radiance measurements with the minimum scattering angle $\Theta = 3^\circ$. The recent CEReS system has introduced a QC control for setting the optimal value of SVA for each site including Uchiyama's method, but no other sub-networks implement these correction methods in their operational analysis.

Though not performed routinely, a Xe-lamp scan has been performed in CEReS for the current version of the sky radiometer (Manago et al., 2016). The merit of the method is that we can narrow the size of the point source below 0.5° and can extend the CSD size beyond $\pm 1^\circ$ without significant effect of the sky light. Then, measured SVAs were compared with those derived from the solar disk scan in daytime. From the experiments, uncertainty in SVA was estimated to be less than ± 0.01 msr or $\pm 4\%$ (Irie et al., 2019). This value is larger than that of Uchiyama et al. (2018b) and more experiments may be needed for more precise estimates and a unit variety.

5. Retrievals of parameters for atmospheric constituents

Once the values of radiometer calibration constants, F_0 and SVA, are determined by the calibration methods described in the preceding two sections, the geophysical parameters of aerosols, clouds, water vapor and ozone are retrieved by inversion of F and/or R in Eqs. (2a) and (2c) at full or specific scattering angles (Fig. 3). Aerosol retrievals are done using Skyrad pack version 4.2 and/or version 5. The former is based on inversion scheme of the Phillips-Twomey type solution of the first kind of Fredholm integral equation with homogeneous smoothing constraint and the latter is based on the second kind of the equation with inhomogeneous constraint with a priori climate data for aerosols (Twomey, 1963) to retrieve the inherent aerosol optical properties. These methods can be generalized by minimization of a cost function ϕ for realization of an observation vector \mathbf{y} as a function of a state vector \mathbf{x} with observation error \mathbf{e} by a multi-term least square method (LSM) (Dubovik and King, 2000; Dubovik, 2004, Dubovik et al., 2011),

$$\mathbf{y} = \mathbf{f}(\mathbf{x}) + \mathbf{e}, \quad (21a)$$

$$\phi = \mathbf{e}'\mathbf{S}_e^{-1}\mathbf{e} + \phi_1 + \phi_2, \quad (21b)$$

$$\phi_1 = (\mathbf{x} - \mathbf{x}_a)'\mathbf{S}_a^{-1}(\mathbf{x} - \mathbf{x}_a), \quad \phi_2 = \mathbf{x}'\mathbf{G}\mathbf{x}, \quad (21c)$$

where superscript t stands for matrix transpose operation, \mathbf{S}_e is the error covariance matrix, ϕ_1 is the norm of the solution from the a priori data \mathbf{x}_a with its associated covariance \mathbf{S}_a . ϕ_2 is a cost for smoothness of the solution with \mathbf{G} matrix related with the norm of the second derivatives of \mathbf{x} . The AERONET analysis uses both the constraints, ϕ_1 and ϕ_2 , but with only two elements for ϕ_1 at the smallest and largest size bins and with the value at the largest size bin as small as to give a contribution to AOT440 wavelength (Dubovik et al., 2006). Skyrad pack versions 4.2 and 5 respectively adopt a third and second term of rhs Eq. (21b), but not both. The latter case of version 5 corresponds to the Maximum a Posteriori solution (MAP) based on the Bayesian theorem (Rodgers, 2000). The MRI version of Skyrad pack uses a ϕ_1 constraint similar to version 5. An iterative search of the nonlinear solution is made by the Gauss-Newton method as

$$\mathbf{x}_{i+1} = \mathbf{x}_i + (\mathbf{K}_i'\mathbf{S}_e^{-1}\mathbf{K}_i + \mathbf{S}_a^{-1} + \mathbf{G})^{-1}[\mathbf{K}_i'\mathbf{S}_e^{-1}(\mathbf{y} - \mathbf{f}(\mathbf{x}_i)) - \mathbf{S}_a^{-1}(\mathbf{x}_i - \mathbf{x}_a) - \mathbf{G}\mathbf{x}_i], \quad (22a)$$

$$\mathbf{K}_i = \nabla_{\mathbf{x}}\mathbf{F}(\mathbf{x})\Big|_{\mathbf{x}=\mathbf{x}_i}. \quad (22b)$$

The version 4.2 uses Eq. (22a) without \mathbf{S}_a terms and the version 5 uses the one without \mathbf{G} terms. Observation and state vectors are given as:

$$\mathbf{y} = \{\tau_a(\lambda_i), R(\lambda_i, \theta_j, \phi_j)\}_{i=1, \dots, N_\lambda; j=1, \dots, N_a}, \quad (23a)$$

$$\mathbf{x} = \{\ln(V_j), \ln(\tilde{n}_r(\lambda_i), \ln \tilde{n}_i(\lambda_i) | i = 1, \dots, N_\lambda; j = 1, \dots, N_v)\}. \quad (23b)$$

where geophysical parameters for the state vector are aerosol volume SDF as a function of logarithm of particle radius r , $x = \ln r$, and real and imaginary parts of CRI, i.e. $\tilde{n} = \tilde{n}_r - \tilde{n}_i i$, as functions of wavelength. The SDF is represented by a linear combinations of base functions

5 $\{f_k\}$,

$$v(x) \equiv \frac{dV}{dx} = \sum_{k=1}^{N_v} V_k f_k(x), \quad x = \ln r. \quad (24a)$$

The package allows two types of base functions, i.e. box-car functions or log-normal functions with mode radii $\{x_k\}$ regularly spaced in x -axis,

$$f_k(x) = \frac{1}{\sqrt{2\pi\sigma}} \exp\left[-\frac{1}{2}\left(\frac{x-x_k}{\sigma}\right)^2\right]. \quad (24b)$$

10 The standard analysis in sub-networks assumes twenty log-normal base functions ($N_v = 20$) from $r = 0.02 \mu\text{m}$ to $20 \mu\text{m}$ with dispersion $\sigma = 0.4$, though there is a discussion for a narrower value (Momoi et al., 2020). A priori value of the CRI is usually given as $\tilde{n} = 1.5 - 0.005i$. The version 4.2 retrieves \mathbf{x} through the following four steps: (Step-1) The SDF for \mathbf{x}_a are assumed to be a bimodal log-normal size distributions ($N_v = 2$) with $r_1 = 0.1 \mu\text{m}$, $r_2 = 2 \mu\text{m}$, and $\sigma_1 = 0.4$, $\sigma_2 =$
 15 0.8 , and volumes of the two modes are set as same, $V_1 = V_2$, and estimated from the forward radiance data ($\Theta \leq 30^\circ$). (Step-2) Retrieve \tilde{n}_r from the radiance data in ($20^\circ, 70^\circ$). (Step-3) Retrieve $\{V_k\}$ from the forward radiance data to revise \mathbf{x}_a . (Step 4) Retrieve SDF and CRI from the full angle scan data. The step 4 is iterated until a conversion criteria is fulfilled. On the other hand, the version 5 follows Step-1, 2, and 4 without step-3. The standard analysis at
 20 sub-networks does not treat asphericity of mineral dust and sea-salt particles and assumes Mie particles, other than in research studies.

The package adopts the IMS method for solar aureole radiance calculation (Nakajima and Tanaka, 1988) for full scalar radiative transfer code, Rstar, with polarization correction by Ogawa et al. (1989) to save computing time. A full polarization vector code, Pstar (Ota et al.,
 25 2010), is also used for research purpose (e.g., Momoi et al., 2020). Asphericity is treated by an approximation of Pollack and Cuzzi (1980) and by several aspherical kernels. Those softwares are available at OpenCLASTR. Other than polar region measurements, the surface albedo is prefixed as 0.05 or 0.1 at wavelengths shorter than 400nm and 0.1 at longer wavelengths.

Figure 8(a) and Table 5 compare observed AOT values with those of AERONET at four
 30 co-located sites of Chiba/Japan, Pune/India, Valencia/Spain, and Seoul/Korea (Khatri et al. 2016). They found RMSDs were 0.019 at 675nm and about 0.015 at 870nm and 1020nm with some site dependence as 0.010, 0.033, 0.009, and 0.022 at 870nm at the four sites, respectively,

though not shown in a table. Che et al.(2008) compared the AOTs between POM-02 skyradiometer and Cimel CE-318 sunphotometer at the top of Institute of Atmospheric Physics(IAP) in Beijing which belongs to SKYNET and AERONET respectively. The POM-02 data were processed by Skyrad pack 4.2. They found RMSD of 0.025 at 440nm and 0.018 at other wavelengths, which are similar to those of Khatri et al, even with the mean AOT at this site as large as 0.33 at 675nm. RMSDs of the Ångström exponent were 0.19 between 440nm and 870nm and 0.28 between 500nm and 870nm, though not shown in a table,.

SKYNET instruments are regularly compared with Precision Filter Radiometer (PFR) instruments belonging to the World optical depth Research and Calibration center (WORCC) and the Global Atmospheric Watch PFR network. Results of three POM instruments compared with the reference WORCC triad in 2015 showed differences less than 0.005 and 0.01 in all cases and for 500nm and 865 nm respectively during the 4th filter radiometer comparison (Kazadzis et al., 2018a). At the same campaign Ångström exponent mean differences were less than 0.5. Under low aerosol conditions, a small relative bias in the AOT determination at 500nm and 865nm can theoretically lead to large deviations in the calculated Ångström Exponents (AE). As an example, for AODs of about 0.05 and 0.02 at 500 and 865 nm, respectively, AOT differences of 0.01 and 0.005, respectively, can lead to AE differences up to ~1. Since 2015 PFR vs POM long-term comparisons have been performed at various stations, i.e. Valencia/Spain, Chiba/Japan, Davos/Switzerland and in the QUATRAM campaign at Rome/Italy (Kazadzis et al., 2018a; personal communication by Campanelli). Figure 8(b) and Table 5 compare AOTs at Davos from those of PMOD PFR . The PFR comparison uses the result from SUNRAD pack (Estelles et at., 2012a) where only direct measurements from the sky radiometer are used to retrieve AOT, having an higher time resolution with respect to direct measurement performed during the almucantar scenarios. They found RMSD as small as 0.007 and 0.001at 500nm and 870nm, respectively.

Using multi-radiometer observation data since 2016 at Yonsei University, Korea in a validation study for the upcoming Geostationary Environment Monitoring Satellite (GEMS) (Kim et al., 2020), Go et al. (2020) compared AOTs from Cimel sunphotometer, Ultraviolet Multifilter Rotating Shadowband Radiometer (UV-MFRSR), NASA Pandora sun spectrometer, and POM-02 sky radiometer. As shown in Table 5, they found RMSDs between AOT values from POM-02 and Cimel sunphotometer as 0.029 to 0.036 for $\lambda \leq 440\text{nm}$ and 0.009 to 0.015 for $\lambda \geq 500\text{nm}$.

Those statistics shown in Table 5 indicate that the RMSD took a value less than 0.02 for $\lambda \geq 500\text{nm}$ and a larger value about 0.03 for shorter wavelengths in city areas, whereas mountain comparisons show smaller RMSDs less than 0.01. This location difference can be understood

by F_0 uncertainties around from 0.5% to 2.4% in Tokyo and Rome and smaller values around 0.3% to 0.5% at the mountain sites of IOA and Davos as discussed in Section 3, though uncertainties in AOT comparisons can include other error sources, such as pointing error, time variation and errors in the retrieval software. Estellés et al. (2012b) discussed this point by comparison of AERONET AOT values with those retrieved by their SUNRAD pack for the same sunphotometer, but with two different analysis modes, i.e. mode-1 which implements the SKYNET extinction model and mode-2 with AERONET-like model. As listed in Table 5, they found RMSD about 0.01 for $\lambda \geq 440\text{nm}$ and larger value in UV channels with mode-1 setup, whereas mode-2 setup give a very small RMSD less than 0.005. Therefore more than half of the RMSDs found in the comparison between SKYNET and AERONET can be attributed to differences in the analysis software. Skyrad pack assumes a simplified extinction model with a plane parallel assumption in the optical airmass formula, ignores water vapor absorption in IR channels, and the ozone absorption extinction model in the UV channels is different from the AERONET model. Slightly larger values at 1020nm than at 875nm may be due to omitting water vapor absorption. Further work is needed to study the effects of these simplifications, which need improvements. For example, SKYNET poses an IL operation limit as $m_0 \leq 3$, instead of $m_0 < 5$ in the data analysis of Estellés et al. (2012b) shown in Table 5.

Table 6 lists reported SSA differences from other networks. SSA values from SKYNET are known to be overestimated as pointed out by Che et al. (2008). Mean values of SSA in Beijing retrieved from the PREDE skyradiometer were significantly larger than those from the Cimel sunphotometer, with differences reaching 0.06 to 0.07 for $\lambda \geq 870\text{nm}$, whereas the mean differences were less than 0.03 at shorter wavelengths. This wavelength dependence can be understood by a tendency of error to increase with decreasing AOT (Dubovik et al., 2000). Similarly Khatri et al. (2016) had a positive difference of about 0.07 RMSD for $\lambda \geq 675\text{nm}$ from AERONET values at the four sites (Chiba, Pune, Valencia, and Seoul). And they found the values can be reduced to around 0.03, if various corrections are applied. The major error source was SVA underestimation of 1.4% to 3.7% causing an SSA increase of 0.03 to 0.04. There were AOT underestimation of 0.02 RMSD at 675nm, as shown in Table 5, which caused an SSA increase of 0.02 at 675nm and less than 0.004 at longer wavelengths. Version 4.2 of Skyrad pack tended to give larger SSA than version 5, but the difference was less than 0.01 for usual aerosol conditions in their case. Effects of surface albedo and asphericity to the SSA difference were less than 0.01. These effects are consistent with those obtained by sensitivity simulations by Pandithurai et al. (2008) and Hashimoto et al. (2012) in a similar way to one described by Dubovik et al (2000). Pandithurai et al. found errors such as 5% error in F_0 , SVA and 0.5 ° error in azimuth angle pointing in SKYNET which can induce an error of 0.03 in retrieved AOT and

mean and maximum differences in retrieved SSA are about 0.004 and 0.02. Hashimoto et al. found in a numerical simulation at 500nm as shown in Table 6, i.e. a positive SSA retrieval error of +0.03 can be caused by SVA underestimation of about 5%, AOT underestimation of about -0.02, and ground albedo underestimation of about -0.1.

5 Aerosol properties in the UV spectral region were extensively measured in the KORUS-AQ campaign (<https://espo.nasa.gov/korus-aq/content/KORUS-AQ>). Mok et al. (2018) compared SSA retrievals as shown in Fig. 9 and Table 6 from SKYNET SR-CEReS, AERONET, and Pandora AMP radiometers from April to August 2016 at Yonsei University, Korea. They found differences around 0.02 for $\lambda \leq 500\text{nm}$ and a larger value as 0.05 at 870nm as similar to those of
10 Che et al. (2008) and Khatri et al. (2016) shown in Table 6. They also found that the SSA difference increased by 0.004 to 0.008 in short wavelengths when they adopted a spectrally fixed ground albedo A_g at 0.1 assumed in the SKYNET analysis, instead of original setup of spectrally varying AERONET ground albedo A_g .

Cloud contamination is another significant error source as studied by Hashimoto et al.
15 (2012). They studied a case of cirrus contamination detected by a lidar observation in Beijing, and found that Skyrad pack version 4.2 retrieved SSA values larger by 0.017 to 0.035 than those from version 5 as shown in Table 6. Version 4.2 simply retrieves a cloud particle volume as coarse mode aerosol volume with the smoothness constraint ϕ_2 in Eq. (21), but the version 5 can filter out the cloud particles owing to a priori constraint ϕ_1 on SDF. This robustness of
20 version 5 to cloud contamination makes the inversion of the aerosol SDF robust to various noises as reported by Che et al. (2014) and Jiang et al. (2019) who demonstrated a clear aerosol bimodal size distribution over Beijing in China by using Skyrad pack version 5. Hashimoto et al. (2012), therefore, proposed a data screening protocol to reject unusually large coarse particle volume: (C1) $\text{AOT}_{500} < 0.4$, (C2) $\varepsilon_r < 0.07$, and (C3) $2 \times V_{2.4\mu\text{m}} < \max(V_{7.7\mu\text{m}}, V_{11.3\mu\text{m}}, V_{16.5\mu\text{m}})$.
25 Application of this screening protocol reduced SSAs by version 4.2 closer to version 5 and AERONET values within 0.03 for eight to nine month data at Pune (India) and Beijing (China).

It is also interesting to compare the sky radiometer method with other methods. Kim et al. (2004, 2005) compared SSAs from a sky radiometer with those estimated by the diffuse direct method (King and Herman, 1976) using data from a collocated pyranometer network in the
30 APEX campaign (Asian Atmospheric Particle Environmental Change Studies) (Nakajima et al., 2003). This method is especially beneficial for the climate study community, because the method gives effective SSA values consistent with the earth radiation budget. They found RMSD at 500nm about 0.03 from data in Amami-Oshima Island. This value is consistent with other values in Table 6.

One reservation about the SSA retrieval by version 5, though, is that it tends to underestimate the SSA due to underestimation of the coarse aerosols when the a priori SDF for constraint tends to zero for radii larger than 10 μ m. Hashimoto et al. (2012) showed by their numerical simulation of an enhanced mineral dust case that the version 5 tends to underestimate SSA by 0.017 to 0.035 compared to version 4.2, as shown in Table 6, because the version 5 mistakenly filter out coarse aerosols by the a priori SDF data \mathbf{x}_a in Eq. (21c). Estellés et al. (2018) found similar underestimation of the coarse aerosols by version 5 compared to aircraft in-situ observations (Marenco et al., 2018; Ryder et al., 2018) for African dust events in the sunphotometer Airborne Validation Experiment in Dust (SAVEX-D) campaign during 16-25 August 2015 as shown in Fig. 10. The figure indicates the version 4.2 retrieved coarse mode SDF similar to the observed one though the error bar is large. These examples suggest an improvement of the a priori SDF data is needed for severe dust storm cases.

Water vapor amount is retrieved from direct solar irradiance measurement in the 940nm channel. F_0 -value in the water vapor channel is retrieved by the modified Langley plot (ML or MLP) method based on the following OT formula instead of Eq. (3),

$$y = \ln F_0 - a_g x, \quad (25a)$$

$$y = \ln F + m(\tau_a + \tau_R), \quad x = (m_g C_g)^{b_g}, \quad (25b)$$

where τ_a and τ_R are AOT and OT for molecular scattering, respectively, and C_g is the column-integrated burden of gaseous species, i.e., PWV W in this case; m_g is optical air mass for the gaseous species; a_g and b_g are two prescribed constants to approximate the beam transmittance due to the gaseous species; a_g can be regarded as an equivalent absorption coefficient for band-averaged absorption of the gaseous species. It is common to assume m_g to be as that of atmospheric air mass, i.e., $m_g = m$ in the water vapor case. The value of τ_a is obtained by an interpolation of the AOT spectrum retrieved from the non-gas absorption channels. There are two algorithms for the SKYNET analysis. One is to use the measured spectral response function of the interference filter of the sky radiometer to prescribe values of a_g and b_g by the theoretical absorption calculation (Uchiyama et al., 2014). This method is similar to that of the AERONET method. The strong line absorption theory of the 930nm spectral band yields $b_g = 0.5$ (Goody and Yung, 1989) in Eq. (25b). However, there is some dependence of b_g on the vertical structure of the atmosphere, so that an improved method is proposed by Campanelli et al. (2010, 2014, 2018) to determine a_g and b_g values by a statistical regression technique of daily observation data at the site. They obtained a range of b_g value as 0.53 to 0.61 as monthly mean values of three years from 2007 to 2009 at San Pietro Capofiume

site (SPC; 44° 23' N, 11° 22' E, 11 m MSL), Italy, with some seasonal dependence. One complexity of this method, though, is a need for measurements of W for making the regression analysis. They used PWV either from radiosonde data or a proxy of PWV constructed from surface meteorological data of temperature and relative humidity. Figure 11 compares PWV by the two methods with GPS and AERONET retrievals in Tsukuba, Japan and Valencia, Spain for data taken in 2011. The figure shows RMSD from validation data is less than 0.2 cm by both the methods, with some systematic underestimation of the slope of the regression line of 10% in the former method. Estellés et al. (2012b) compared PWV at Valencia, Spain between AERONET values and those retrieved by SUNRAD pack for a same Cimel sunphotometer. They found RMSD of 0.20 cm when SUNRAD pack uses mode-1 (SKYNET-like) setup, whereas it is reduced to 0.17 cm if SUNRAD uses mode-2 (AERONET-like) setup, indicating performances of the two modes are similar to each other in water vapor retrievals, compared to a significant difference in the AOT case as shown in Table 5 .

In order to get rid of the F_0 retrieval process in the water vapor channel, Momoi et al. (2020) proposed a new method of using water vapor dependence of the relative radiance along the almucantar circle of the sky. Although this method has a limited range of retrievable PWV less than 2 cm, there is a merit in using the value from the method, say W_{sky} , as a proxy of $C_g = W$ in Eq. (25b) to perform the MLP on site, similar to the IL method for the non-absorption channels, but with

$$x = W_{sky}^{b_g}, \quad (26)$$

instead of Eq. (25b).

The columnar ozone amount (O_3) is retrieved from the direct solar irradiance measurement of 315 nm channel for the Huggins band. Khatri et al. (2014) determined the F_0 -value by a ML method Eq. (26) assuming $b_g=1$ for ozone without a significant line absorption structure. The formula of m_g is given by Robinson (1966). In the F_0 determination process, they simultaneously obtained an optimal value of the equivalent ozone absorption coefficient a_g which bring the slope of the ML plot to unity using data of ozone column burden $C_g = U$ measured by the Dobson spectrometer. RMSD of the fitting for a campaign data at Tsukuba site from 13 December, 2012 to 8 January, 2013 was 13 Dobson Unit (DU) as shown in Fig. 12. They also reported a large degradation of filter transmission in the ozone channel.

Cloud microphysical properties have been obtained from diffuse sky radiance measurements from satellites (Nakajima and King, 1990). Similar approach can be applied to the ground-based radiance measurements. Chiu et al. (2010, 2012) retrieved cloud optical thickness (COT) and effective particle radius (CER) from AERONET data. SKYNET uses the

POM-02 sky radiometer which has 1.6 μm and 2.2 μm channels (Kikuchi et al., 2006; Khatri et al., 2019). Figure 13 compares COT retrieved from POM-02 at zenith observations at the three sites of Chiba, Fukue and Hedo combined with retrievals from Himawari-8/AHI satellite-borne imager in a period of October 2015 to December 2016 (Khatri et al., 2019). Satellite retrieval results were obtained by the Comprehensive Analysis Program for Cloud Optical Measurement (CAPCOM) (Nakajima and Nakajima, 1995) in the system of AMATERASS (Takenaka et al., 2011; Damiani et al., 2018). Geostationary satellite observation has a merit of frequent time-matching with the ground-based observation. The figure shows there is a large scatter of RMSD as 10.2 and a correlation of 0.89. They also studied cloud effective particle radius, but did not find a significant correlation between SKYNET and AHI observations. Figure 14 also compares the broad-band radiance at zenith measured by a ground-based pyrliometer and with broad-band horizontal radiative flux measured by a pyranometer with those theoretically calculated using the cloud parameters from sky radiometer measurement. The figure indicates that the down-welling radiance at zenith was consistent between the two radiometers, but horizontal radiative flux were not well represented by the cloud optical properties retrieved from the sky radiometer at nadir. Figures 13 and 14 suggest that the inhomogeneity of cloud fields is a main source of differences between the cloud parameters obtained by the sky radiometer and satellite measurements.

6. Conclusions

The SKYNET community has undertaken efforts for improving the on-site calibration and analysis systems to provide retrieved aerosol and other atmospheric constituents.

An estimate of the retrieval accuracy of F_0 is given by Eq. (10) for the IL method, which can serve as an approximation to observed monthly mean uncertainty in F_0 as 0.5% to 2.4 % in Tokyo and Rome sites and smaller values around 0.3% to 0.5% at the mountain sites of IOA and Davos. These values are consistent with RMSD values in the AOT comparisons with other networks less than 0.02 for $\lambda \geq 500\text{nm}$ and a larger value about 0.03 for shorter wavelengths in city areas, and smaller values less than 0.01 in mountain comparisons. We also developed a new XIL method to correct an underestimation by the IL method in case of large aerosol retrieval errors.

Several causes of larger SSA values reaching 0.07 than those of other networks have been identified as underestimation of SVA measured by the disk scan method and a new lamp scan method, cloud contamination, and others. Recent reported values of the difference are found to be less than 0.03 after these corrections.

Retrievals of other atmospheric constituents by the sky radiometer are also reviewed. We found accuracies of about 0.2 cm for the precipitable water vapor amount and 13 Dobson Units for the column ozone amount. A new on-site calibration method for water vapor has been developed. The cloud optical properties were found to have some but not large correlation with satellite remote sensing values, suggesting cloud inhomogeneity may be one source of error.

There are several aims for the next step of the SKYNET to make its system more reliable and useful for the science community. The reported useful improvements of the product quality are still in research phase and important to be introduced in the existing operational systems and future system of the ISDC. Also comparison studies showed that the analysis software Skyrad pack may need improvements in its simplified optical model. We want to pursue our on-site calibration system for sustainable operation of the network. However, continuous comparison of on-site calibrations of our standard sky radiometer with high mountain calibrations.

15 **Acknowledgments**

We are grateful for support by projects of JAXA SGLI, MOEJ-JAXA GOSAT and GOSAT2, ERCA/ERDF/S-12, JST/CREST/TEEDDA (JPMJCR15K4). Prof. K. Miura of Tokyo University of Science are gratefully acknowledged for providing us with Langley plot data. A part of co-authors were supported by ERCA/ERDF/2-1901, JSPS/KAKENHI/JP19H04235, P17K00529, and the JAXA 2nd research announcement on the Earth Observations (grant number 19RT000351).

ESR thanks: the support of Spanish Ministry of Economy and Competitiveness and European Regional Development Fund through funding to the University of Valencia within several projects, such as CGL2015-70432-R and CGL2017-86966-R; ESR thanks Dr. Costantini of the Research Area of TorVergata for the data center and server maintenance. The SAVEX-D campaign was funded by EUFAR TNA (European Union Seventh Framework Programme grant agreement 312609), making use of airborne data obtained using the BAe-146-301 Atmospheric Research Aircraft operated by Airtask Ltd and managed by the Facility for Airborne Atmospheric Measurements (FAAM). It was a success thanks to many staff at the Met Office, the University of Leeds, Manchester and Hertsfordshire, FAAM, Directflight Ltd, Avalon Engineering and BAE Systems.

JK was supported by the “Technology development for Practical Applications of Multi-Satellite data to maritime issues” funded by the Ministry of Ocean and Fisheries, Korea.

We thank to Alexander Smirnov of NASA GSFC for useful discussion on the history of sun and sky measurements.

References

- Abbot, C. G.: The silver disk pyrheliometer, *Smithson. Misc. Collect.*, 56(19), 11pp., 1911.
- Abbot, C. G., and Aldrich, L. B.: The pyranometer- An instrument for measuring sky radiation,
5 *Smithson. Misc. Collect.*, 66(7), 9pp., 1916.
- Ångström, A. K.: Techniques of determining the turbidity of the atmosphere, *Tellus*, 13,
214-223, 1961.
- Ångström, A. K.: Circumsolar sky radiation and turbidity of the atmosphere, *Appl. Opt.*, 13,
474-477, 1974.
- 10 de Bary, E.: Influence of multiple scattering of the intensity and polarization of diffuse sky
radiation, *Appl. Opt.*, 3, 1293-1303, 1964.
- Boi, P., Tonna, G., Dalu, G., Nakajima, T., Olivieri, B., Pompei, A., Campanelli, M., and Rao,
R.: Calibration and data elaboration procedure for sky irradiance measurements, *Appl. Opt.*,
38, 896–907, doi:10.1364/AO.38.000896, 1999.
- 15 Box, M. A., and Deepak, A.: Single and multiple scattering contributions to circumsolar
radiation, *Appl. Opt.*, 17, 3794-3797, 1978.
- Box, M. A., and Deepak, A.: Retrieval of aerosol size distributions by inversion of simulated
aureole data in the presence of multiple scattering, *Appl. Opt.*, 18, 1376-1382, 1979.
- Bullrich, K., Scattered radiation in the atmosphere and the natural aerosol, *Advances in*
20 *Geophysics*, 10, 99-260, 1964.
- Bullrich, K., Eiden, R., and Nowak, W.: Sky Radiation, polarization and twilight radiation in
Greenland, *Pure Appl. Geophys.*, 64, 220-242, 1967.
- Bullrich, K., Eiden, R., Jaenicke, R., and Nowak, W.: Solar radiation extinction, sky radiation,
sky light polarization and aerosol particle total number and size distribution on the Island
25 Maui (Hawaii), *Pure Appl. Geophys.*, 69, 280-319.1968.
- Campanelli, M., Nakajima, T., and Olivieri, B.: Determination of the solar calibration constant
for a sun sky radiometer. Proposal of an in situ procedure, *Appl. Opt.*, 43, 651-659, 2004.
- Campanelli, M., Estellés, V., Tomasi, C., Nakajima, T., Malvestuto, V., and Martínez-Lozano,
J. A.: Application of the SKYRAD improved Langley plot method for the in situ calibration
30 of CIMEL sun-skphotometers, *Appl. Opt.*, 46, 2688-2702, 2007.
- Campanelli, M., Lupi, A., Nakajima, T., Malvestuto, V., Tomasi, C., and Estelles, V.:
Summertime columnar content of atmospheric water vapor from ground-based Sun-sky
radiometer measurements through a new in situ procedure, *J. Geophys. Res.*, 115, D19304,
doi:10.1029/2009JD013211, 2010.

- Campanelli, M., Estelles, V., Smyth, T., Tomasi, C., Martinez-Lozano, M. P., Claxton, B., Muller, P., Pappalardo, G., Pietruczuk, A., Shanklin, J., Colwell, S., Wrench, C., Lupi, A., Mazzola, M., Lanconelli, C., Vitale, V., Congeduti, F., Dionisi, D., Cardillo, F., Cacciani, M., Casasanta, G., and Nakajima, T.: Monitoring of Eyjafjallajokull volcanic aerosol by the new European Skynet Radiometers (ESR) network, *Atmos. Environ.*, 48, 33-45, doi: 10.1016/j.atmosenv.2011.09.070, 2012.
- Campanelli, M., Nakajima, T., Khatri, P., Takamura, T., Uchiyama, A., Estelles, V., Liberti, G. L., and Malvestuto, V.: Retrieval of characteristic parameters for water vapour transmittance in the development of ground based Sun-Sky radiometric measurements of columnar water vapour, *Atmos. Meas. Tech.*, 7, 1075–1087, doi:10.5194/amt-7-1075-2014, 2014.
- Campanelli, M., Mascitelli, A., San`o, P., Diémoz, H., Estellés, V., Federico, S., Iannarelli, A. M., Fratarcangeli, F., Mazzoni, A., Realini, E., Crespi, M., Bock, O., Martínez-Lozano, J. A., and Dietrich, S.: Precipitable water vapour content from ESR/SKYNET sun-sky radiometers: validation against GNSS/GPS and AERONET over three different sites in Europe, *Atmos. Meas. Tech.*, 11, 81-94, 2018.
- Che, H., Shi, G., Uchiyama, A., Yamazaki, A., Chen, H., Goloub, P., and Zhang, X.: Intercomparison between aerosol optical properties by a PREDE skyradiometer and CIMEL sunphotometer over Beijing, China, *Atmos. Chem. Phys.*, 8, 3199–3214, doi:10.5194/acp-8-3199-2008, 2008.
- Che, H., Shi, G., Zhao, H., Nakajima, T., Khatri, P., Takamura, T., Wang, H., Wang, Y., Sun, J., and Zhang, X.: Aerosol optical properties retrieved from a Prede sky radiometer over an urban site of Beijing, China, *J. Meteorol. Soc. Japan*, 92A, 17–31, doi: 10.2151/jmsj.2014-A02, 2014.
- Chiu, J.-C., Huang, C.-H., Marshak, A., Slutsker, I., Giles, D. M., Holben, B., Knyazikhin, Y., and Wiscombe, W.: Cloud optical depth retrievals from the Aerosol Robotic Network (AERONET) cloud mode observations, *J. Geophys. Res.*, 115, doi 10.1029/2009JD013121, 2010.
- Chiu, J. C., Marshak, A., Huang, C.-H., Várnai, T., Hogan, R. J., Giles, D. M., Holben, B. N., O'Connor, E. J., Knyazikhin, Y., and Wiscombe, W. J.: Cloud droplet size and liquid water path retrievals from zenith radiance measurements: examples from the Atmospheric Radiation Measurement Program and the Aerosol Robotic Network, *Atmos. Chem. Phys.*, 12, 10313-10329, <https://doi.org/10.5194/acp-12-10313-2012>, 2012, 2012.
- Damiani, A., Irie, H., Horio, T., Takamura, T., Khatri, P., Takenaka, H., Nagao, T., Nakajima, T. Y., and Cordero, R. R.: Evaluation of Himawari-8 surface downwelling solar radiation by ground-based measurements, *Atmos. Meas. Tech.*, 11, 2501-2521, 2018.

- Dave, J. D.: Determination of size distribution of spherical polydispersions using scattered radiation data, *Appl. Opt.*, 10, 2035-2044, 1971.
- Deirmendjian, D.: Theory of the solar aureole Part I: Scattering and radiative transfer, *Annales de Géophysiqu*, 13, 286-306, 1957.
- 5 Deirmendjian, D.: Theory of the solar aureole Part II: Applications to atmospheric models, *Annales de Géophysiqu*, 15, 218-249, 1959.
- Dubovik, O.: Optimization of Numerical Inversion in Photopolarimetric Remote Sensing, in *Photopolarimetry in Remote Sensing*, edited by: Videen, G., Yatskiv, Y., and Mishchenko, M., Kluwer Academic Publishers, Dordrecht, Netherlands, 65–106, 2004.
- 10 Dubovik, O., and King, M. D.: A flexible inversion algorithm for retrieval of aerosol optical properties from Sun and sky radiative measurements, *J. Geophys. Res.*, 105, 20673–20696, 2000.
- Dubovik, O., Smirnov, A., Holben, B., King, M. D., Kaufman, Y. J., Eck, T. F., and Slutsker, I.: Accuracy assessment of aerosol optical properties retrieval from Aerosol Robotic Network (AERONET) Sun and sky radiance measurements, *J. Geophys. Res.*, 105, 9791–9806, 2000.
- 15 Dubovik, O., Holben, B., Eck, T. F., Smirnov, A., Kaufman, Y. J., King, M. D., Tanré, D., and Slutsker, I.: Variability of absorption and optical properties of key aerosol types observed in worldwide locations, *J. Geophys. Res.*, 59, 590-608, 2002.
- Dubovik, O., Sinyuk, A., Lapyonok, T., Holben, B. N., Mishchenko, M., Yang, P., Eck, T. F., 20 Volten, H., Muñoz, O., Veihelmann, B., van der Zande, W. J., Leon, J. F., Sorokin, M., and Slutsker, I.: Application of spheroid models to account for aerosol particle nonsphericity in remote sensing of desert dust, *J. Geophys. Res.*, 111, D11208, 2006.
- Dubovik, O., Herman, M., Holdak, A., Lapyonok, T., Tanré, D., Deuzé, J. L., Ducos, F., Sinyuk, A., and Lopatin, A.: Statistically optimized inversion algorithm for enhanced retrieval of 25 aerosol properties from spectral multi-angle polarimetric satellite observations, *Atmos. Meas. Tech.*, 4, 975–1018, doi:10.5194/amt-4-975-2011, 2011.
- Eiden, R.: Calculations and measurements of the spectral radiance of the solar aureole, *Tellus*, 20, 380-399, 1968.
- Estellés, V., Campanelli, M., Smyth, T. J., Utrillas, M. P., and Martínez-Lozano, J. A.: 30 AERONET and ESR sun direct products comparison performed on Cimel CE318 and Prede POM01 solar radiometers, *Atmos. Chem. Physics Discuss.* 12, 4341-4371, doi:10.5194/acpd-12-4341-2012, 2012a.
- Estellés, V., Campanelli, M., Smyth, T. J., Utrillas, M. P., and Martínez-Lozano, J. A.: Evaluation of the new ESR network software for the retrieval of direct sun products from

- CIMEL CE318 and PREDE POM01 sun-sky radiometers, *Atmos. Chem. Phys.*, 12, 11619–11630, 2012, doi:10.5194/acp-12-11619-2012, 2012b.
- Estellés, V., Marenco, F., Ryder, C., Segura, S., O’ sullivan, D., Brooke, J., Campanelli, M., Buxmann, J., and Martínez-Lozano, J. A.: Validation of AERONET and ESR/SKYNET size distributions with airborne insitu measurements in dust conditions. 9th International Workshop on Sand/Duststorms and Associated Dustfall, 22-24 May, Tenerife, Spain, 2018.
- 5 Fesenkov, V.G.: To the question of solar constant determination, *Sov. Astron. J.*, 10(3), 249–266, 1933.
- Giles, D. M., Sinyuk, A., Sorokin, M. G., Schafer J. S., Smirnov, A., Slutsker, I., Eck, T. F., Holben, B. N., Lewis, J. R., Campbell, J. R., Welton, E. J., Korokin, S. V., and Lyapustin, A. I.: Advancements in the Aerosol Robotic Network (AERONET) Version 3 database-automated near-real-time quality control algorithm with improved cloud screening for sun photometer aerosol optical depth (AOD) measurements, *Atmos. Meas. Tech.*, 12, 169-209, doi.org/10.5194/amt-12-169-2019.
- 10 Go, S., Kim, J., Mok, J., Irie, H., Yoon, J., Torres, O., Krotkov, N. A., Labow, G., Kim, M., Koo, J.-H., Choi, M., and Lim, H.: Ground-based retrievals of aerosol column absorption in the UV spectral region and their implications for GEMS measurements, *Remote Sens. Environ.*, 245, 111759, doi.org/10.1016/j.rse.2020.111759, 2020.
- Gorodetskiy, A. K., Katin, V. S., and Petrenko, B. Z., The transparency of the atmosphere and the scattering phase function from aircraft measurements at 1.9-2.3 μm , *Izv. Atmos. Ocean Phys.*, 12, 1269-1276, 1976.
- 20 Green, A. E. S., Deepak, A., and Lipofsky, B.J.: Interpretation of the sun's aureole based on atmospheric models, *Appl. Opt.*, 10, 1263-1279, 1971.
- Goody, R.M. and Yung, Y.L.: *Atmospheric Radiation*, Second ed., Oxford Univ. Press, New York, Oxford., 286pp, 1989.
- 25 Hashimoto, M., Nakajima, T., Dubovik, O., Campanelli, M., Che, H., Khatri, P., Takamura, T., and Pandithurai, G.: Development of a new data processing method for the SKYNET skyradiometer observation, *Atmos. Meas. Tech.*, 5, 2723-2737, doi:10.5194/amt-5-2723-2012, 2012.
- 30 Holben, B. N., Eck, T. F., Slutsker, I., Tanré, D., Buis, J. P., Setzer, A., Vermote, E., Reagan, J. A., Kaufman, Y. J., Nakajima, T., Lavenue, F., Jankowiak, I., and Smirnov, A.: AERONET – A federated instrument network and data archive for aerosol characterization, *Remote Sens. Environ.*, 66, 1–16, 1998.
- Holben, B. N., Tanré, D., Smirnov, A., Eck, T. F., Slutsker, I., Abuhassan, N., Newcomb, W.W., Schafer, J.S., Chatenet, B., Lavenue, F., Kaufman, Y.J., Vande Castle, J., Setzer, A.,
- 35

- Markham, B., Clark, D., Frouin, R., Halthore, R., Karneli, A., O'Neill, N. T., Pietras, C., Pinker, R. T., Voss, K., and Zibordi, G.: An emerging ground-based aerosol climatology: Aerosol optical depth from AERONET, *J. Geophys. Res.*, 106, 12067-12097, 2001.
- Hoyt, D. V.: The Smithsonian Astrophysical Observatory solar constant program, *Rev. Geophys. Space Phys.*, 17, 427-458, 1979a.
- Hoyt, D. V.: Pyrheliometric and circumsolar sky radiation measurements by the Smithsonian Astrophysical Observatory from 1923 to 1954, *Tellus*, 31, 217-229, 1979b.
- Jiang, Z., Duan, M., Che, H., Zhang, W., Nakajima, T., Hashimoto, M., Chen, B., and Yamazaki, A.: Inter-comparison between the Aerosol Optical Properties Retrieved by Different Inversion Methods from SKYNET Sky Radiometer Observations over Qionghai and Yucheng in China, *Atmos. Meas. Tech. Discuss.*, <https://doi.org/10.5194/amt-2019-39>, in review, 2019.
- Irie, H., Hoque, H. M. S., Damiani, A., Okamoto, H., Fatmi, A. M., Khatri, P., Takamura, T., and Jarupongsakul, T.: Simultaneous observations by sky radiometer and MAX-DOAS for characterization of biomass burning plumes in central Thailand in January–April 2016, *Atmos. Meas. Tech.*, 12, 599–606, 2019, <https://doi.org/10.5194/amt-12-599-2019>, 2019.
- Kalitin, N. N., To the question of studying sky radiation intensity around the Sun, *Bulletin of Constant Actinometric Commission of Main Geophysical Observatory*, 1, 51-56, 1930 (in Russian).
- Kaufman, Y. J., G. P. Gobbi, and I. Koren: Aerosol climatology using a tunable spectral variability, cloud screening of AERONET data, *Geophys. Res. Lett.*, 33, L07817, doi: 10.1029/2005GL025478, 2006.
- Kazadzis, S., Kouremeti, N., Diémoz, H., Gröbner, J., Forgan, B. W., Campanelli, M., Estellés, V., Lantz, K., Michalsky, J., Carlund, T., Cuevas, E., Toledano, C., Becker, R., Nyeki, S., Kosmopoulos, P.G., Tatsiankou, V., Vuilleumier, L., Denn, F. M., Ohkawara, N., Ijima, O., Goloub, P., Raptis, P.I., Milner, M., Behrens, K., Barreto, A., Martucci, G., Hall, E., Wendell, J., Fabbri, B.E., and Wehrli, C.: Results from the Fourth WMO Filter Radiometer Comparison for aerosol optical depth measurements, *Atmos. Chem. Phys.*, 18, 3185-3201, <https://doi.org/10.5194/acp-18-3185-2018>, 2018a.
- Kazadzis, S., Kouremeti, N., Nyeki, S., Gröbner, J., and Wehrli, C.: The World Optical Depth Research and Calibration Center (WORCC) quality assurance and quality control of GAW-PFR AOD measurements, *Geosci. Instrum. Method. Data Syst.*, 7, 39-53, <https://doi.org/10.5194/gi-7-39-2018>, 2018b.
- Khatri, P. and Takamura, T.: An algorithm to screen cloud-affected data for sky radiometer data analysis, *J. Meteorol Soc. Japan*, 87, 189-204, 2009.

- Khatri P., Takamura, T., Shimizu, A., and Sugimoto, N.: Spectral dependency of aerosol light-absorption over the East China Sea region, *SOLA*, 6, 1–4, doi:10.2151/sola.2010-001, 2010.
- 5 Khatri, P., Takamura, T., Yamazaki, A., and Uchiyama, A.: Use of 315 nm channel data of the sky radiometer to estimate the columnar ozone concentration: A preliminary study, *J. Meteorol. Soc. Japan*, 92A, 185-194, doi:10.2151/jmsj.2014-A12, 2014.
- Khatri, P., Takamura, T., Nakajima, T., Estellés, V., Irie, H., Kuze, H., Campanelli, M., Sinyuk, A., Lee, S.-M., Sohn, B. J., Pandithurai, G., Kim, S.-W., Yoon, S. C., Martinez-Lozano, J. A., Hashimoto, M., Devara, P. C. S., and Manago, N.: Factors for inconsistent aerosol single scattering albedo between SKYNET and AERONET, *J. Geophys. Res. Atmos.*, 121, 1859–1877, doi:10.1002/2015JD023976, 2016.
- 10 Khatri, P., Iwabuchi, H., Hayasaka, T., Irie, H., Takamura, T., Yamazaki, A., Damiani, A., Letu, H., and Kai, Q.: Retrieval of cloud properties from sky radiometer observed spectral zenith radiances, *Atmos. Meas. Tech.*, 12, 6037-6047, doi:10.5194/amt-12-6037-2019.
- 15 Kikuchi, N., Nakajima, T., Kumagai, H., Kuroiwa, H., Kamei, A., Nakamura, R., and Nakajima, T. Y.: Cloud optical thickness and effective particle radius derived from transmitted solar radiation measurements: Comparison with cloud radar observations, *J. Geophys. Res.*, 111, D07205, doi:10.1029/2005JD006363, 2006.
- Kim, D.-H., Sohn, B.-J., Nakajima, T., Takamura, T., Takemura, T., Choi, B.-C., and Yoon, S.-C.: Aerosol optical properties over East Asia determined from ground-based sky radiation measurements, *J. Geophys. Res.*, 109, No. D2, D02209, doi:10.1029/2003JD003387, 2004.
- 20 Kim, D.-H., Sohn, B.-J., Nakajima, T., and Takamura, T.: Aerosol radiative forcing over East Asia determined from ground-based solar radiation measurements, *J. Geophys. Res.*, 110, D10S22, doi:10.1029/2004JD004678, 2005.
- 25 Kim, J., et al.: New era of air quality monitoring from space, *Geostationary Environment Monitoring Spectrometer (GEMS)*, *Bull. Amer. Meteorol. Soc.*, January 2020, <https://doi.org/10.1175/BAMS-D-18-0013.1>, 2020.
- King, M. D., and Herman, B. M.: Determination of the ground albedo and the index of absorption of atmospheric particulates by remote sensing. part I: Theory, *J. Atmos. Sci.*, 36, 163–173, 1979.
- 30 Kobayashi, E., Uchiyama, A., Yamazaki, A., and Matsuse, K.: Application of the statistical optimization method to the inversion algorithm for analyzing aerosol optical properties from sun and sky radiance measurements, *J. Meteor. Soc. Japan*, 84, 1047-1062, 2006.
- Kobayashi, E., Uchiyama, A., Yamazaki, A., and Kudo, R.: Retrieval of aerosol optical properties based on the spheroidal model. *J. Meteor. Soc. Japan*, 88, 847-856, 2010.
- 35

- Kobayashi, H., and Shiobara, M.: Development of new shipborne aureolemeter to measure the intensities of direct and scattered solar radiation on rolling and pitching vessel, Proc. SPIE 9640, Remote Sensing of Clouds and the Atmosphere XX, **9640**, 1A 1-9, 2015.
- Manago, N., Khatri, P., Irie, H., Takamura, T., and Kuze, H.: On the method of solid view angle calibration for SKYNET skyradiometers, *4th International SKYNET workshop*, Rome, Italy, 2–4 March, 2016.
- Marenco, F., Ryder, C., Estellés, V., O'Sullivan, D., Brooke, J., Orgill, L., Lloyd, G., and Gallagher, M.: Unexpected vertical structure of the Saharan Air Layer and giant dust particles during AER-D, *Atmos. Chem. Phys.*, 18, 17655–17668, <https://doi.org/10.5194/acp-18-17655-2018>.
- Mok, J., Krotkov, N.A., Torres, O., Jethva, H., Li, Z., Kim, J., Koo, J.-H., Go, S., Irie, H., Labow, G., Eck, T. F., Holben, B. N., Herman, J., Loughman, R. P., Spinei, E., Lee, S. S., Khatri, P., and Campanelli, M.: Comparisons of spectral aerosol single scattering albedo in Seoul, South Korea, *Atmos. Meas. Tech.*, 11, 2295–2311, 2018.
- Momoi, M., Kudo, R., Aoki, K., Mori, T., Miura, K., Okamoto, H., Irie, H., Shoji, Y., Uchiyama, A., Ijima, O., Takano, M., and Nakajima, T.: Development of an on-site self-calibration and retrieval methods of precipitable water vapor for sky-radiometer observations, *Atmos. Meas. Tech.*, 13, 2635-2658, doi.org/10.5194/amt-13-2635-2020.
- Murai, K.: Spectral measurements of direct solar radiation and of sun's aureole (I), *Papers in Meteorology and Geophysics*, 18, 3, 239-291, 1967.
- Nakajima, T., Tanaka, M., and Yamauchi, T.: Retrieval of the optical properties of aerosols from aureole and extinction data. *Appl. Opt.*, 22, 2951-2959, 1983.
- Nakajima, T., Tanaka, M., Hayasaka, T., Miyake, Y., Nakanishi, Y., and Sasamoto, K.: Airborne measurements of the optical stratification of aerosols in turbid atmospheres, *Appl. Opt.*, 25, 4374-4381, 1986.
- Nakajima, T., and Tanaka, M.: Algorithms for radiative intensity calculations in moderately thick atmospheres using a truncation approximation, *J. Quant. Spectrosc. Radiat. Transfer*, 40, 51-69, doi: 10.1016/0022-4073(88)90031-3, 1988.
- Nakajima, T., and M. D. King, 1990: Determination of the optical thickness and effective radius of clouds from reflected solar radiation measurements. Part I: Theory. *J. Atmos. Sci.*, **47**, 1878-1893.
- Nakajima, T., Tonna, G., Rao, R., Kaufman, Y., and Holben, B.: Use of sky brightness measurements from ground for remote sensing of particulate polydispersions, *App. Opt.*, 35, 2672-2686, doi: 10.1364/AO.35.002672, 1996.

- Nakajima, T., Sekiguchi, M., Takemura, T., Uno, I., Higurashi, A., Kim, D.H., Sohn, B.J., Oh, S.N., Nakajima, T.Y., Ohta, S., Okada, I., Takamura, T., and Kawamoto, K.: Significance of direct and indirect radiative forcings of aerosols in the East China Sea region. *J. Geophys. Res.*, 108(D23), 8658, doi: 10.1029/2002JD003261, 2003.
- 5 Nakajima, T., Yoon, S.-C., Ramanathan, V., Shi, G.-Y., Takemura, T., Higurashi, A., Takamura, T., Aoki, K., Sohn, B.-J., Kim, S.-W., Tsuruta, H., Sugimoto, N., Shimizu, A., Tanimoto, H., Sawa, Y., Lin, N.-H., Lee, C.-T., Goto, D., and Schutgens, N.: Overview of the Atmospheric Brown Cloud East Asian Regional Experiment 2005 and a study of the aerosol direct radiative forcing in east Asia, *J. Geophys. Res.*, 112, D24S91, doi:10.1029/2007JD009009, 2007.
- 10 Nakajima, T. Y., and Nakajima, T.: Wide-area determination of cloud microphysical properties from NOAA AVHRR measurements for FIRE and ASTEX regions, *J. Atmos. Sci.*, 52, 4043-4059, doi: 10.1175/1520-0469(1995)052<4043:WADOCM>2.0.CO;2, 1995.
- Ningombam, S.S., Bagare, S.P., Singh, R.B., Campanelli, M., Khatri, P., Dorjey, N.: Calibration of a Sky radiometer (Prede) using observations obtained from Hanle and Merak high-altitude stations, *Atmos. Res.*, 143, 118–128, 2014.
- 15 Ogawa, H., Tanaka, M., and Nakajima, T.: A simple expression for the additional sky radiance produced by polarization effects, *J. Meteor. Soc. Japan*, 67, 877-888, 1989.
- O'Neill, N. T. and Miller, J. R.: Combined solar aureole and solar beam extinction measurements. 1: Calibration considerations, *Appl. Opt.*, 23, 3691-3696, 1984a.
- 20 O'Neill, N. T. and Miller, J. R.: Combined solar aureole and solar beam extinction measurements. 2: Studies of the inferred aerosol size distribution, *Appl. Opt.*, 23, 3697-3703, 1984b.
- Ota, Y., Higurashi, A., Nakajima, T., and Yokota, T.: Matrix formulations of radiative transfer including the polarization effect in a coupled atmosphere-ocean system. *J. Quant. Spectrosc. Radiat. Transfer*, 111, 878-894, doi:10.1016/j.jqsrt.2009.11.021, 2010.
- 25 Pandithurai, G., Dipu, S., Dani, K. K., Tiwari, S., Bisht, D. S., Devara, P. C. S., and Pinker, R. T.: Aerosol radiative forcing during dust events over New Delhi, India, *J. Geophys. Res.*, 113, D13209, doi:10.1029/2008JD009804, 2008.
- 30 Phillips, D.L.: A technique for the numerical solution of certain integral equations of the first kind, *J. Ass. Comp. Mech.*, 9, 84-97, 1962.
- Pollack, J. B. , and Cuzzi, J. N.: Scattering by nonspherical particles of size comparable to a wavelength: A new semi-empirical theory and its application to tropospheric aerosols, *J. Atmos. Sci.*, 37, 868-881, 1980.

- Pyaskovskaya-Fesenkova, E.V., Investigations of atmospheric scattering light, Acad. Sci. USSR, Moscow, 218pp, 1957.
- Ramanathan, V., Li, F., Ramana, M. V., Praveen, P. S., Kim, D., Corrigan, C. E., Nguyen, H., Stone, E. A., Schauer, J. J., Carmichael, G. R., Adhikary, B., and Yoon, S.C.: Atmospheric brown clouds: Hemispherical and regional variations in long range transport, absorption and radiative forcing, *J. Geophys. Res.*, 112, D22S21, doi:10.1029/2006JD008124, 2007.
- Robinson, N.: *Solar Radiation*, Elsevier, Amsterdam, 347pp, 1966.
- Rodgers, C. D.: *Inverse Method for Atmospheric Sounding*, World Sci., Singapore, 256 pp, 2000.
- 10 Roosen, R. G., Angione, R. J., and Clemcke C. H.: Worldwide variations in atmospheric transmission, Baseline results from Smithsonian observations, *Bull. Amer. Meteorol. Soc.*, 54, 307-316, 1973.
- Ryder, C.L., Marengo, F., Brooke, J.K., Estelles, V., Cotton, R., Formenti, P., McQuaid, J.B., Price, H.C., Liu, D., Ausset, P., Rosenberg, P. D., Taylor, J. W., Choularton, T., Bower, K., 15 Coe, H., Gallagher, M., Crosier, J., Lloyd, G., Highwood, E. J., and Murray, B. J.: Coarse-mode mineral dust size distributions, composition and optical properties from AER-D aircraft measurements over the tropical eastern Atlantic, *Atmos. Chem. Phys.*, 18, 17225–17257, 2018, <https://doi.org/10.5194/acp-18-17225-2018>.
- Shaw, G. E.: Error analysis of multi-wavelength sun photometry, *Pure Appl. Geophys.*, 114, 20 390-395, 1976.
- Shaw, G. E.: Genesis of sun photometry, *Proc. SPIE 6362, Remote Sensing of Clouds and the Atmosphere XI*, 636201, doi: 10.1117/12.692771, 2006.
- Shifrin, K. S., Turchin, V.F., Turovtseva, L. S., and Gashko, V. A.: Reconstruction of particle size distribution by statistical regularization of the scattering function, *Izv. Atmos. Ocean Phys.*, 8, 739-743, 1972.
- 25 Shifrin, K. S., and Gashko, V. A.: Reconstruction of the particle size distribution functions when the information about the refractive index of the particles is inexact, *Izv. Atmos. Ocean Phys.*, 10, 943-949, 1974.
- Smirnov, A., Holben, B. N., Eck, T. F., Dubovik, O., and Slutsker, I.: Cloud-screening and quality control algorithms for the AERONET data- base, *Remote Sens. Environ.*, 73, 337–349, 2000.
- 30 Song, H. J., Sohn, B. J., Chun, H. W., Chun, Y., and Lee, S. S.: Improved cloud screening method for the analysis of sky radiometer measurements and application to Asian dust detection, *J. Meteorol. Soc. Japan*, 92A, 167-183, 2014.

- Takamura, T., Nakajima, T., and SKYNET community group: Overview of SKYNET and its activities, *Opt. Pura Apl.*, 37, 3303–3308, 2004.
- Takamura, T., Takenaka, H., Cui, Y., Nakajima, T. Y., Higurashi, A., Fukuda, S., Kikuchi, N., Nakajima, T., Sato, I., and Pinker, R. T.: Aerosol and cloud validation system based on SKYNET observations: Estimation of shortwave radiation budget using ADEOS-II/GLI data, *J. Remote Sens. Japan*, 29, 40-53, 2009.
- Takamura, T., Khatri, P., Sohn, B. J., Tugjsuren, N., Tana, B., Campanelli, M., and Pandihurai, G.: Aerosol optical properties and aerosol direct effects over typical sites of SKYNET network. International Conference book on climate change in arid and semi-arid regions, 91-98, Ulaanbaatar, Mongolia, ISBN 978-99973-823-5-1, 2013.
- Takenaka, H., Nakajima, T. Y., Higurashi, A., Higuchi, A., Takamura, T., Pinker, R. T., and Nakajima, T.: Estimation of solar radiation using a neural network based on radiative transfer, *J. Geophys. Res.*, 116, D08215, doi:10.1029/2009JD013337, 2011.
- Tanaka, M., Nakajima, T., and Shiobara, M.: Calibration of a sunphotometer by simultaneous measurements of direct-solar and circumsolar radiations, *Appl. Opt.*, 25, 1170-1176, 1986.
- Tanré, D., Devaux, C., Herman, M. and Santer, R.: Radiative properties of desert aerosols by optical ground-based measurements at solar wavelengths, *J. Geophys. Res.*, 93, 14223-14231, 1988.
- Terez, E. I., and G. A. Terez: A method to determine atmospheric optical depth using observations of direct solar radiation, *J. Geophys. Res.*, 108, No. D22, 4704, doi:10.1029/2003JD003829, 2003.
- Tonna, G., Nakajima, T., and Rao, R.: Aerosol features retrieved from solar aureole data: A simulation study concerning a turbid atmosphere, *Appl. Opt.*, 34, 4486-4499, 1995.
- Turchin, V. F., and Nozik, V. Z.: Statistical regularization of the solution of incorrectly posed problems, *Izv. Atmos. Ocean. Phys. (English Ed.)*, 5, 14-18, 1969.
- Twitty, J.T.: The inversion of aureole measurements to derive aerosol size distributions. *J. Atmos. Sci.*, 32, 584-591, 1975.
- Twitty, J.T., Parent, R.J., Weinman, J. A., and Eloranta, E. W.: Aerosol size distribution: remote determination from airborne measurements of the solar aureole, *Appl. Opt.*, 15, 980-989, 1976.
- Twomey, S.: On the numerical solution of Fredholm integral equations of the first kind by the inversion of the linear system produced by quadrature, *J. Ass. Comp. Mech.*, 10, 97-101, 1963.
- Uchiyama, A., Yamazaki, A., and Kudo, R.: Column water vapor retrievals from sky radiometer (POM-02) 940 nm data, *J. Meteorol. Soc. Japan*, 92A, 195-203, 2014.

- Uchiyama, A., Matsunaga, T., and Yamazaki, A.: The instrument constant of sky radiometer (POM-02) - Part 1: Calibration constant, *Atmos. Meas. Tech.*, 11, 5363-5388, <https://doi.org/10.5194/amt-11-5363-2018>, 2018a.
- 5 Uchiyama, A., Matsunaga, T., and Yamazaki, A.: The instrument constant of sky radiometer (POM-02) - Part 2: Solid view angle, *Atmos. Meas. Tech.*, 11, 5389-5402, <https://doi.org/10.5194/amt-11-5363-2018>, 2018b.
- Uchiyama, A., Shiobara, M., Kobayashi, H., Matsunaga, T., Yamazaki, A., Inei, K., Kawai, K., and Watanabe, Y.: Nocturnal aerosol optical depth measurements with modified skyradiometer POM-02 using the moon as a light source, *Atmos. Meas. Tech. Discuss.*, <https://doi.org/10.5194/amt-2019-230>, in review, 2019.
- 10 Volz, F. E.: Photometer mit Selen-Photoelement zur spektralen Messung der Sonnenstrahlung und zur Bestimmung der Wellenlängenabhängigkeit der Dunsttrübung, *Arch. Meteor. Geophys. Bioklimatol.*, B10, 100–131, 1959.
- Volz, F. E.: Economical Multispectral Sun Photometer for Measurements of Aerosol Extinction from 0.44 μm to 1.6 μm and Precipitable Water, *Applied Optics*, 13, 1732-1733, 1974.
- 15 Weinman, J. A., Twitty, J. T., Browning, S. R., and Herman, B. M.: Derivation of phase functions from multiply scattered sunlight transmitted through a hazy atmosphere, *J. Atmos. Sci.*, **32**, 577-583, 1975.
- 20 Yamamoto, G., and Tanaka, M.: Determination of aerosol size distribution from spectral attenuation measurements, *Appl. Opt.*, 8, 447-453, 1969.

Table and Figure captions

Table 1. Sites recognized by the International Skynet Committee.

Name	Owner	Country	Location (Lat)	Location (Lon)	Location (MSL, m)	Sub-net analyzers	ISDC
Halley	British Antarctic Survey	Antarctica	75.350S	26.340W	30 m	ESR	
Rothera	British Antarctic Survey	Antarctica	67.340S	68.080W	0m	ESR	
Showa	NIPR	Antarctica	69.006S	39.590E	30m	-	x
Chajnantor, Atacama	Universidad de Santiazgo de Chile	Chile	33.451S	70.686W	5100 m	ESR	
Beijing/CAMS	CMA	China	39.933N	116.317E	106m	CAMS	
Beijing/IAP	IAP-CAS	China	39.977N	116.381E	92m	CAS	
Dunhuang	IAP-CAS	China	40.146N	90.799E	1120m	CAS, Chiba-U	
Hefei	AIOFM-CAS	China	31.897N	117.173E	30m	CAS, U-Toyama	
Lanzhou	Lanzhou-U	China	35.570N	104.133E	1965m	Lanzhou-U	
Qionghai	IAP-CAS	China	19.230N	110.46E	24m	CAS	
Xi'an	XAUT	China	34.25N	108.983E	396.9m	XAUT	
Orleans	NIES	France	47.965N	2.113E	131m	Chiba-U	x
Lindenberg	Meteorologisches Observatorium Lindenberg/Mark	Germany	52.209N	14.121E	120 m	ESR	
Amaravati	IMD	India	16.573N	80.358E	343m	IMD	
Aurangabad	IMD	India	19.876N	75.343E	568m	IMD	
Gangtok	IMD	India	27.339N	88.607E	1650m	IMD	
Guwahati	IMD	India	26.100N	91.580E	54m	IMD	
Hanle	Indian Institute of Astrophysics	India	32.779N	78.964E	4500m	IIAP, Chiba-U	x
Hyderabad	National Remote Sensing Agency, India	India	17.469N	78.486E	811m	IMD, U-Toyama	
Jaipur	IMD	India	27.175N	75.955E	431m	IMD	
Jodhpur	IMD	India	26.300N	73.020E	224m	IMD	
Kolkata	IMD	India	22.650N	88.450E	88m	IMD	
Merak	Indian Institute of Astrophysics	India	33.480N	78.360E	4258m	IIAP, Chiba-U	x
Minicoy	IMD	India	8.274N	73.050E	2m	IMD	
Nagpur	IMD	India	21.100N	79.050E	310m	IMD	

New Delhi/IITM	Indian Institute of Tropical Meteorology	India	28.629N	77.174E	240m	IMD, Chiba-U	
New Delhi/IMD	IMD	India	28.580N	77.210E	216m	IMD, U-Toyama	
New Delhi/NPL	National Physical Laboratory, India	India	28.637N	77.174E	223m	IMD, U-Toyama	
Port Blair	IMD	India	11.670N	92.720E	79m	IMD	
Puducherry	IMD	India	11.942N	79.808E	3m	IMD	
Pune/IITM	Indian Institute of Tropical Meteorology	India	18.537N	73.805E	559m	IMD, Chiba-U	
Pune/IMD	IMD	India	18.530N	73.850E	559m	IMD	
Raipur	IMD	India	21.251N	81.630E	298m	IMD	
Ranichauri	IMD	India	30.250N	78.080E	1800m	IMD	
Rohtak	IMD	India	28.830N	76.580E	214m	IMD	
Sagar	IMD	India	23.839N	78.738E	427m	IMD	
Trivandrum	IMD	India	08.480N	76.950E	60m	IMD	
Varanasi	IMD	India	25.300N	83.020E	90m	IMD	
Visakhapatnam	IMD	India	17.720N	83.230E	18m	IMD	
Aosta	ARPA-VDA	Italy	45.742N	7.357E	570 m	ESR	
Bologna	CNR-ISAC	Italy	44.650N	11.650E	8m	Chiba-U	
Bologna	CNR-ISAC	Italy	44.520N	11.340E	60m	Chiba-U	
Messina	Italian Air force	Italy	38.200N	15.500E	0m	ESR	
Monte Cimone	Italian Air force	Italy	44.190N	10.700E	2165 m	ESR	
Novara	Italian Air force	Italy	45.530N	8.670E	169 m	ESR	
Paganella	Italian Air force	Italy	46.110N	11.040E	2129 m	ESR	
Rome	CNR-ISAC	Italy	41.905N	12.548E	70.0m	ESR	
Sigonella	Italian Air force	Italy	37.405 N	14.919 E	30 m	ESR	
Vigna di Valle	Italian Air force	Italy	42.080N	12.210E	270 m	ESR	
Abashiri	U-Toyama	Japan	44.018N	144.280E	45m	U-Toyama	
Chiba	Chiba-U	Japan	35.625N	140.104E	21m	Chiba-U, U-Toyama	x
Etchujima	Tokyo Univ. Marine Sci.	Japan	35.664N	139.796E	35.0m	Chiba-U, U-Toyama	x
Fuji Hokuroku	AIST	Japan	35.433N	138.750E	1150m	Chiba-U, U-Toyama	x
Fukue	Chiba-U	Japan	32.752N	128.682E	80m	Chiba-U, U-Toyama	x
Fukuoka	Kyushu-U	Japan	33.524N	130.475E	28m	Chiba-U, U-Toyama	x
Fukuoka	MRI	Japan	33.552N	130.365E	31m	MRI	
Fussa	U-Toyama	Japan	35.751N	139.323E	141m	U-Toyama	

Hedo	Chiba-U	Japan	26.867N	128.248E	65m	Chiba-U, U-Toyama	x
Ishigaki	JMA	Japan	24.337N	124.164E	6m	JMA	x
Itabashi	Tokyo Kasei Univ.	Japan	35.775N	139.721E	70m	U-Toyama	
Jodo	U-Toyama	Japan	36.566N	137.606E	2839m	U-Toyama	
Kamiyukawa	U-Toyama	Japan	34.062N	135.516E	535m	U-Toyama	
Kanazawa	Kanazawa Institute of Technology	Japan	36.533N	136.629E	26m	U-Toyama	
Kofu	Chiba-U	Japan	35.650N	138.567E	300m	Chiba-U, U-Toyama	x
Minamitorishima	MRI	Japan	24.300N	153.970E	7m	MRI	
Minamitorishima /JMA	JMA	Japan	24.288N	153.983E	7m	JMA	x
Miyakojima	MRI	Japan	24.737N	125.327E	50m	MRI, Chiba-U	
Moshiri	NIES	Japan	44.366N	142.260E	288m	Chiba-U, U-Toyama	x
Nagasaki	Nagasaki-U	Japan	32.786N	129.865E	35m	Chiba-U, U-Toyama	
Okayama	AIST	Japan	34.664N	133.931E	13m	U-Toyama	
Osaka	Kinki-U	Japan	34.642N	135.587E	19m	Chiba-U, U-Toyama	
Saga	Saga-U, NIES	Japan	33.233N	130.283E	8m	Chiba-U	x
Sapporo/ILTS	U-Toyama	Japan	43.084N	141.339E	30m	U-Toyama	
Sapporo/ILTS,MRI	U-Toyama	Japan	43.084N	141.339E	30m	U-Toyama	
Sapporo/JMA	JMA	Japan	43.060N	141.329E	17m	JMA	x
Sendai	Tohoku-U	Japan	38.260N	140.840E	153m	Chiba-U, U-Toyama	x
Shigaraki	U-Toyama	Japan	34.854N	136.105E	295m	U-Toyama	
Suzu, Ishikawa	U-Toyama	Japan	37.451N	137.359E	15m	U-Toyama	
Takayama	Gifu-U	Japan	36.145N	137.423E	1420m	Chiba-U, U-Toyama	x
Takikawa	U-Toyama	Japan	43.547N	141.897E	40m	U-Toyama	
Toyama	U-Toyama	Japan	36.700N	137.187E	30m	U-Toyama	
Tsukuba	Tsukuba-U	Japan	36.114N	140.096E	27m	Chiba-U, U-Toyama	x
Tsukuba/MRI	MRI	Japan	36.056N	140.125E	30m	MRI	
Kagurazaka	Tokyo Univ. of Science	Japan	35.699N	139.741E	70m	-	
Mandargovi	Chiba-U	Mongolia	45.743N	106.264E	1393m	Chiba-U	x

Ulaanbaatar	MUST, Chiba-U	Mongolia	47.886N	106.906E	1350m	Chiba-U	x
Lauder	NIWA, NIES	New Zealand	45.038S	169.681E	370m	Chiba-U	x
Ny-Alesund	NIPR	Norway	78.930N	11.861E	50m	U-Toyama	x
Belsk	Polish Academy of Science	Poland	51.837N	20.792E	190m	ESR, U-Toyama	
Anmyon	SNU	Republic of Korea	36.517N	126.317E	45m	SNU, U-Toyama	
Kongju	Kongju National Univ.	Republic of Korea	36.280N	127.080E	70m	SNU, U-Toyama	
Seoul	SNU	Republic of Korea	37.460N	126.950E	150m	SNU, Chiba-U, U-Toyama	x
Yongin	Hankuk University of Foreign Studies	Republic of Korea	37.336N	127.268E	167m	SNU, U-Toyama	x
Yonsei	Yonsei-U	Republic of Korea	37.570N	126.980E	60m	SNU	x
Barcelona	Universitat de Barcelona	Spain	41.385N	2.118E	97 m	ESR	
Valencia-Burjassot	Universitat de Valencia	Spain	39.507N	0.420W	60 m	ESR, Chiba-U	
Bangkok	TMD	Thailand	13.667N	100.605E	60m	Chiba-U	
Phimai	Chiba-U	Thailand	15.184N	102.565E	212m	Chiba-U, U-Toyama	x
Sri-samrong	Chiba-U	Thailand	17.157N	99.867E	50m	Chiba-U, U-Toyama	
Cambridge	British Antarctic Survey	United Kingdom	52.215N	0.080E	30 m	ESR	
Cardington	Met-Office	United Kingdom	52.100N	0.421W	30 m	ESR	
London	University College London-UAO	United Kingdom	51.524N	0.131W	45 m	ESR	
Plymouth	Plymouth Marine Lab.	United Kingdom	50.366N	4.148W	0m	ESR	
Aurora, Colorado	AIST	USA	39.400N	104.500W	1674 m	ESR	
Golden	National Renewable Energy Laboratory	USA	39.740N	105.180W	1829 m	ESR	

Table 2. Geophysical parameter products, versions of Skyrad pack, and availability of the known data archives.

ESR:<http://www.euroskyrad.net>

L2 products: AOT, AE, SDF, SSA, CRI, phase function, asymmetry factor, lidar ratio and
5 linear depolarization ratio

Analysis software: Skyrad pack v4.2, MRI v2

Data availability: L2 data are open by web system

SR-CEReS: <http://atmos3.cr.chiba-u.jp/skynet/>

L2 products: AOT, AE, SDF, SSA, CRI

10 Analysis software: Skyrad pack v5

Data availability: L2 data are open by web system

Toyama U: <http://skyrad.sci.u-toyama.ac.jp/>

L2 products: AOT, AE, SDF, SSA, CRI

Analysis software: Skyrad pack v4.2, 5

15 Data availability: L2 data are open by individual request

MRI

L2 products: AOT, AE, SDF, SSA, CRI, phase function, asymmetry factor, Lidar ratio,
Linear depolarization ratio

Analysis software: Skyrad pack MRI v1 and v2

20 Data availability: L2 data are available from PIs by request

CAMS-SKYNet

Operational L2 products: AOT, AE, SDF, SSA, CRI

Analysis software: Skyrad pack v4.2 and 5

Data availability: L2 data are used by CMA, data available from PIs by request

25 IMD

Operational L2 products: AOT, AE, SDF, SSA

Analysis software: Skyrad pack v4.2

Data availability: L2 data are used by IMD, no open web system

30

Table 3. (a) Monthly mean values of n , τ_a and $\sigma_{a,IL}$ obtained by ILP at Tokyo University of
Science (TUS) site averaged for a period of February-May 2017 and (b) those at Roman site
averaged for Oct 2017 and May-Sept 2019, other than *380nm data which was taken only in
Oct 2017. Estimates of $\sigma_{a,IL}$ are also given by Eq. (10) assuming γ -value of 7% for Tokyo
35 and 15% for Rome. All wavelength means are shown in the bottom of each table.

(a) Tokyo

λ (nm)	$\langle n \rangle$	$\langle \tau_a \rangle$	$\langle \sigma_{a,IL} \rangle$ (%)	Eq. (10) (%) $\gamma = 7\%$
340	230	0.363	1.43	1.54
380	189	0.343	2.37	1.61
400	223	0.321	1.26	1.38
500	271	0.241	1.02	0.94
675	257	0.159	0.77	0.64
870	184	0.121	0.54	0.57
1020	202	0.100	0.47	0.45
mean	222	0.235	1.12	1.02

(b) Rome

λ (nm)	$\langle n \rangle$	$\langle \tau_a \rangle$	$\langle \sigma_a \rangle$ (%)	Eq. (10) (%) $\gamma = 15\%$
340	360	0.178	1.25	1.29
*380	135	0.099	0.98	1.18
400	366	0.171	1.51	1.23
500	360	0.120	0.87	0.87
675	336	0.081	0.56	0.61
870	321	0.061	0.57	0.47
1020	315	0.057	0.61	0.44
mean	313	0.110	0.91	0.85

Table 4. Estimates a and b values at $\lambda = 500\text{nm}$ and their RMSD values (σ_a , σ_b) in the F_0

5 retrieval by IL and XIL methods for ILP data at Tokyo University of Science (TUS) site for four months from February through May 2017. Results of three screening conditions of Eq. (17) with $\varepsilon_{u0} = 0.05, 0.03, \text{ and } 0.02$ are listed.

$\varepsilon_{u0} = 0.05$				
method	a	σ_a	$-b$	σ_b
SL	-8.220	0.389	0.296	0.321
IL	-8.247	0.050	0.968	0.082
XIL	-8.219	0.069	1.035	0.117
$\varepsilon_{u0} = 0.03$				
method	a	σ_a	$-b$	σ_b
SL	-8.253	0.238	0.237	0.163
IL	-8.249	0.039	0.973	0.070
XIL	-8.233	0.039	1.019	0.073
$\varepsilon_{u0} = 0.02$				
method	a	σ_a	$-b$	σ_b
SL	-8.190	0.168	0.247	0.160
IL	-8.243	0.030	0.990	0.064
XIL	-8.233	0.031	1.025	0.075

10

Table 5. Statistics of AOT differences from other networks. RMSD values of Estellés et al. (2012b) are differences between AERONET values and SUNRAD values for the same Cemil-CE318 sunphotometer data with mode-1 (SKYNET-like) and mode-2 (AERONET-like) algorithms.

5

source	statistics	340	380	440	500	675	870	1020
Che et al. (2008), Beijing w AERONET	mean			0.536	-	0.330	0.248	0.211
	RMSD			0.025	-	0.018	0.018	0.018
Fig.8(a), 4 sites* Khatri et al. (2016) w AERONET	mean					0.124	0.089	0.080
	RMSD					0.019	0.015	0.016
Fig.8(b), Davos Kazadzis et al. (2018a,b) w PFR	mean				0.041	-	0.037	-
	RMSD				0.007	-	0.001	-
Go et al. (2020), Seoul w AERONET	mean	0.263	0.235	0.205	0.173	0.119	0.088	0.087
	RMSD	0.036	0.033	0.029	0.015	0.009	0.007	0.015
Estellés et al. (2012b) Valencia AERONET (mode-1) AERONET (mode-2)	RMSD	0.018	0.013	0.011	0.010	0.010	0.008	0.010
	RMSD	0.005	0.004	0.002	0.002	0.002	0.001	0.002
	RMSD	0.005	0.004	0.002	0.002	0.002	0.001	0.002

* 4 sites: Chiba, Pune, Valencia, Seoul

Table 6. Reported SSA differences from other networks: mean bias (Che et al., 2008) and RMSD (Kim et al., 2005; Khatri et al. 2016; Mok et al., 2018). Simulated changes of SSA between Skyrad pack versions 4.2 and 5 and SSA retrieval errors of version 4.2 in an enhanced mineral dust case are also obtained by a numerical simulation (Hashimoto et al., 2012).

5

source	method	340	380	440 ¹	500	675	870	1020
Kim et al. (2005) rmsd	Diffuse to direct				0.027			
Che et al. (2008) w AERONET, mean				0.01	0.03	0.03	0.06	0.07
Khatri et al. (2016), 4sites ² , w AERONET rmsd	before correction					0.069	0.074	0.068
	after correction					0.027	0.030	0.037
Mok et al. (2018) w AERONET rmsd	spectral Ag	0.017	0.015	0.016	0.025		0.047	
	Ag=0.1	0.025	0.018	0.020	0.024		0.048	
Hashimoto et al. (2012), simulation mean difference	Beijing observed cirrus contamination, v4.2-v5			0.017	0.023	0.029	0.035	0.023
	enhanced mineral dust case, v4.2			0.008	0.004	-0.005	-0.013	-0.017
	v5			-0.013	-0.017	-0.026	-0.031	-0.030

¹400nm in Hashimoto et al. (2012)

²Chiba, Pune, Valencia, Seoul

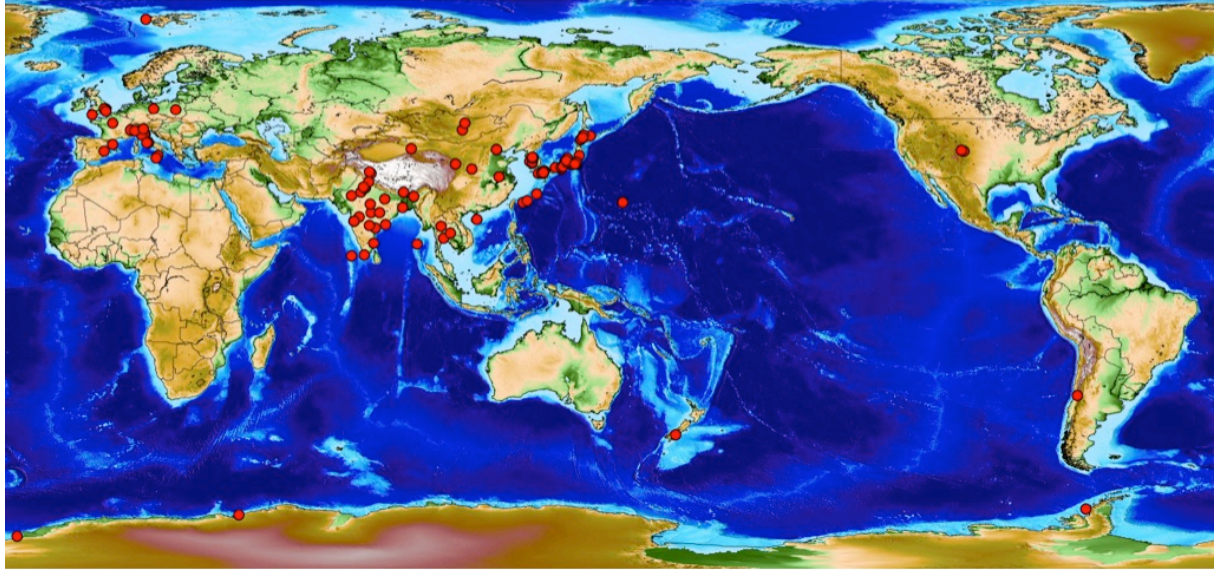


Fig. 1. A map of the sky radiometer sites.

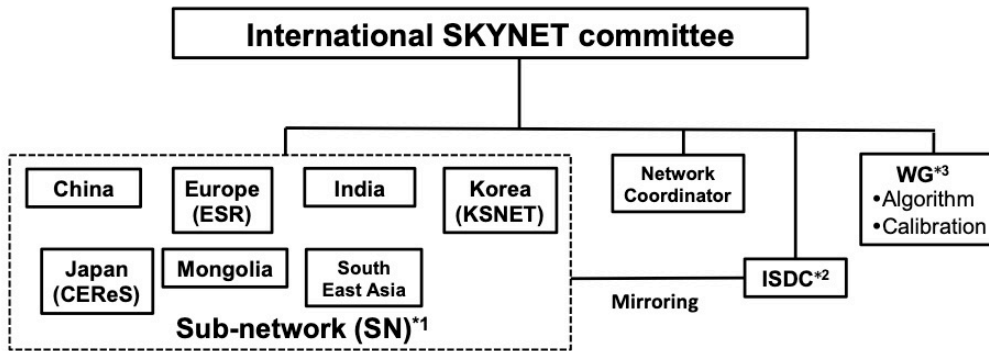


Fig. 2. The structure of the International SKYNET committee.

5

Campaign-base operations

On site operation routines

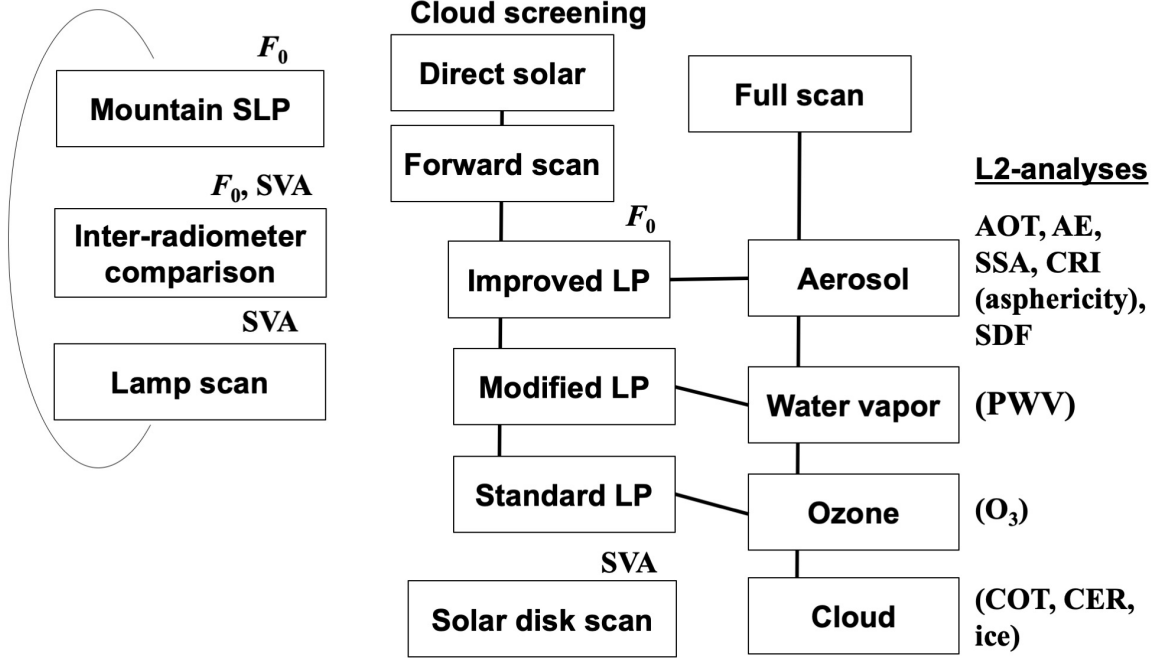
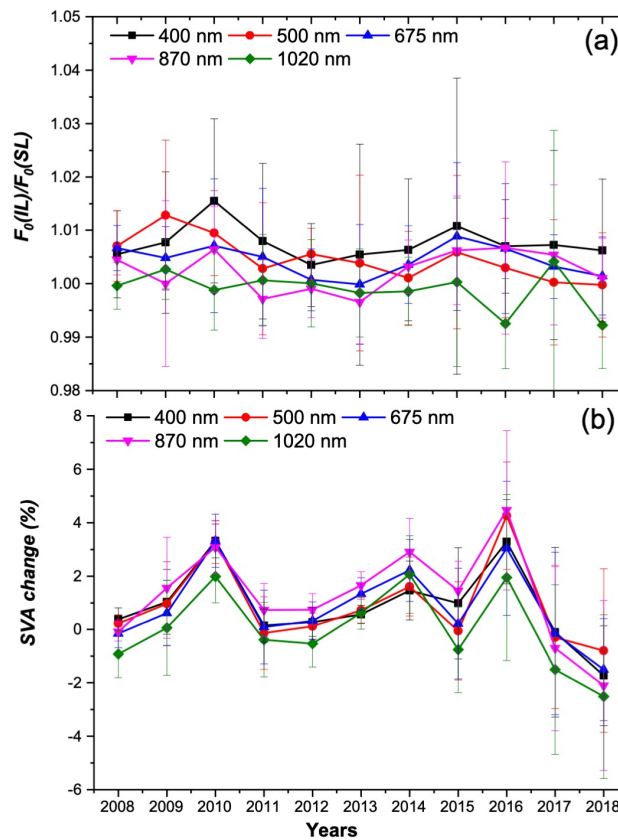
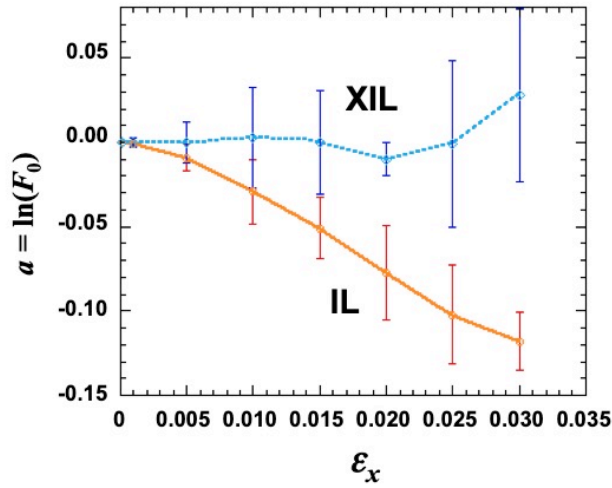


Fig. 3. A flow chart of the SKYNET analysis. Quantities in parentheses are research products.

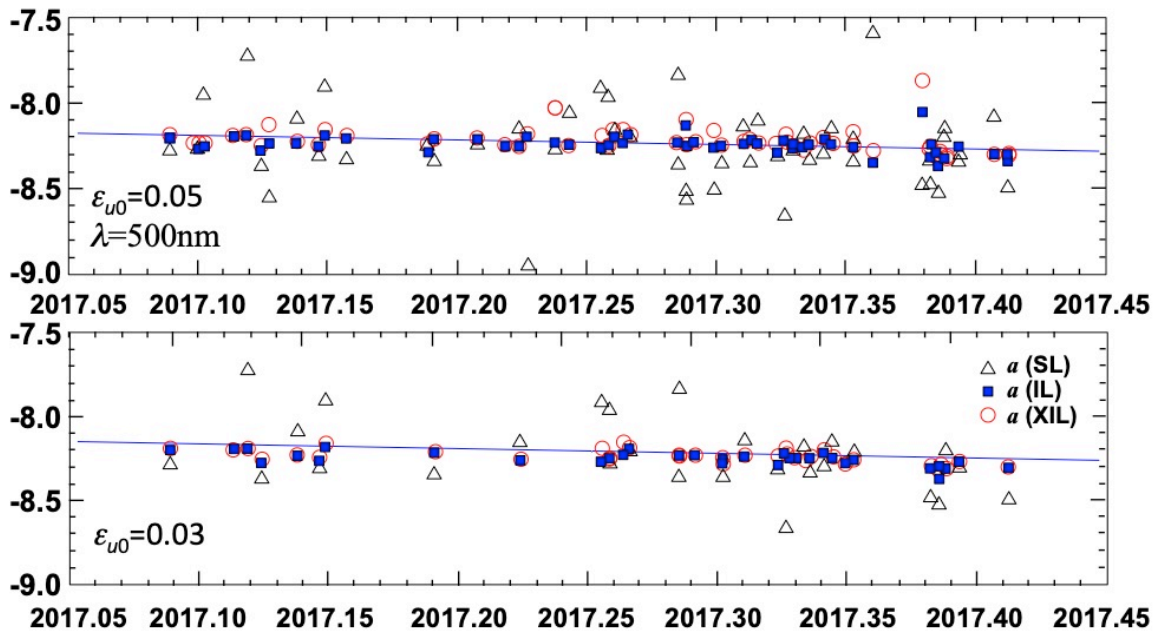


5 Fig. 4. Time series of the ratio of F_0 -values from SL and IL methods (a) and SVA (b) from the observation taken by a single instrument (POM-01) at two pristine sites, IAO-Hanle during

January 2008 - December 2010 and June 2015 - December 2018 and Merak during January 2011 - May 2015. The error bar indicates a representative monthly RMSD in each year.



5 Fig. 5. Retrieved values of $a = \ln(F_0)$ from IL and XIL methods with ten ensemble runs of an idealized experiment ($n=20$ and $m=1.3$ to 3.5) as a function of normal random error ε_x in x . True values are assumed as $F_0=1$, $\omega=1$, $\tau=0.1$.



10 Fig. 6. Time series of estimated a -values by IL and XIL methods for ILP data at Tokyo University of Science (TUS) site for four months from February through May 2017. Presented are results of two screening conditions of Eq. (17) with $\varepsilon_{u0}=0.05$ and 0.03 at $\lambda=500\text{nm}$.

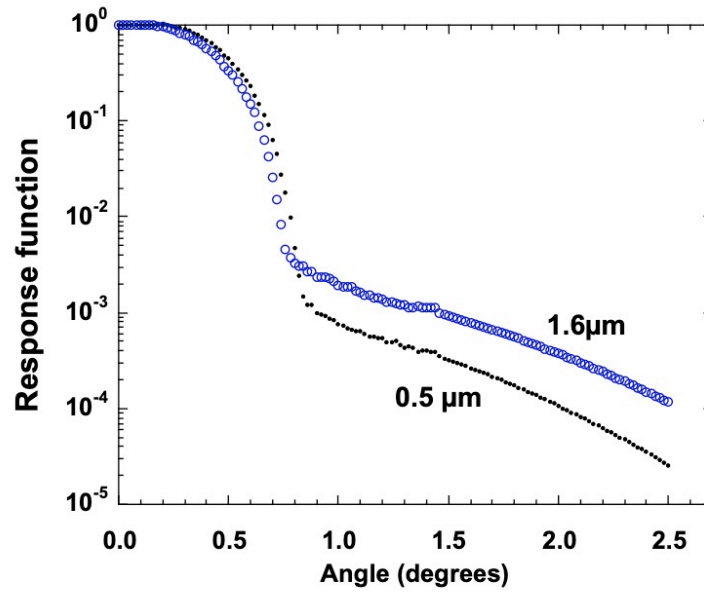


Fig. 7. Response functions of the sky radiometer at $\lambda=0.5 \mu\text{m}$ and $1.6\mu\text{m}$ measured by the solar disk scan method.

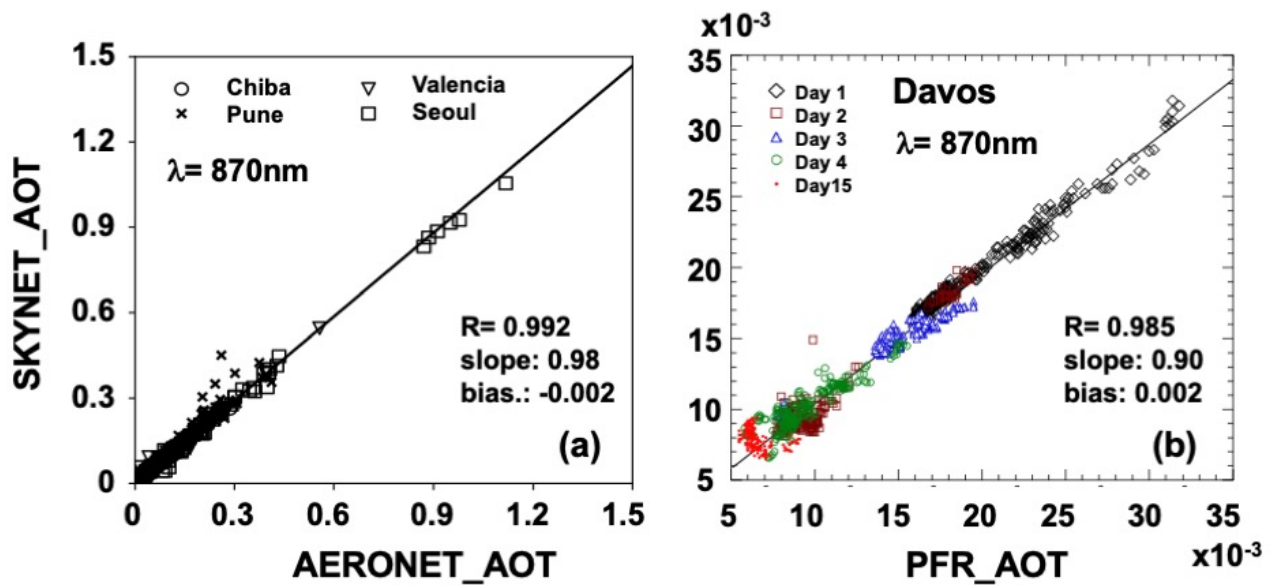


Fig. 8. Comparison of AOT values at $\lambda=870\text{nm}$ obtained by sky radiometer, Cimel sunphotometer and PMOD PFR.

5

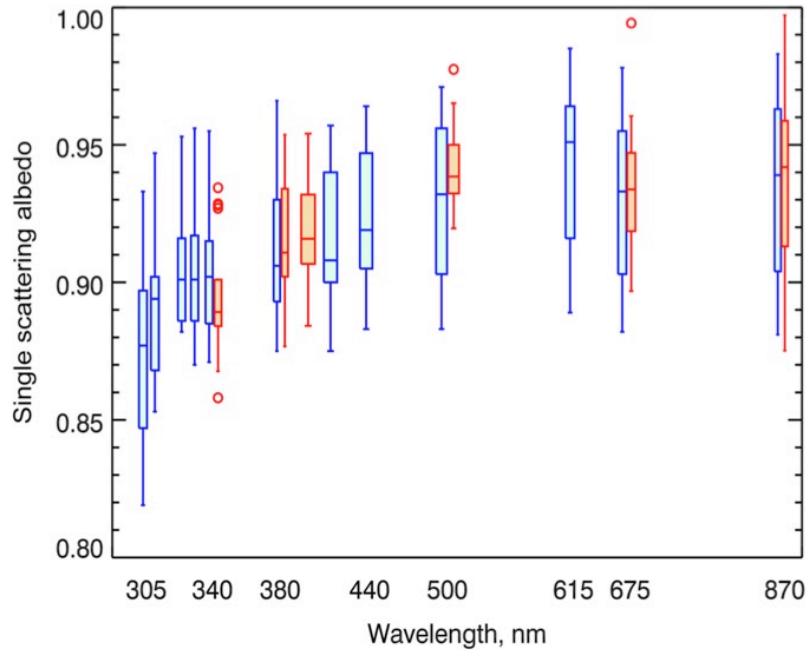
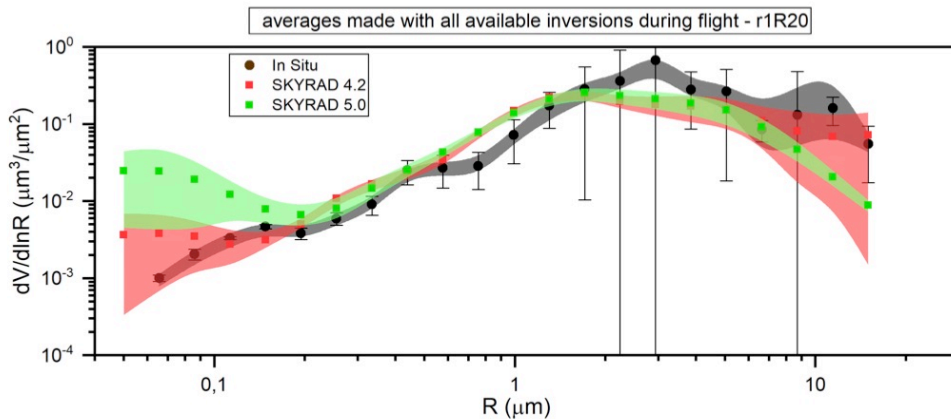


Fig. 9. Combined spectral SSA from AMP-retrievals (blue symbols) and SKYNET retrievals (orange symbols) using MODIS-derived surface albedo. The bottom and top edges of the boxes are located at the sample 25th and 75th percentiles; the whiskers extend to the minimal and maximal values within 1.5 IQR. The outliers are shown in circles. The center horizontal lines are drawn at the median values. The whisker-boxes are computed using $AOD_{440} \geq 0.4$ criteria to correspond the best quality level 2 AERONET data. Cited from Mok et al. (2018).

5



10

Fig. 10. Retrieved and observed aerosol size distribution functions in the African dust event cases in the sunphotometer Airborne Validation Experiment in Dust (SAVEX-D) campaign during 16-25 August 2015 (Estellés et al., 2018; Marengo et al., 2018; Ryder et al., 2018).

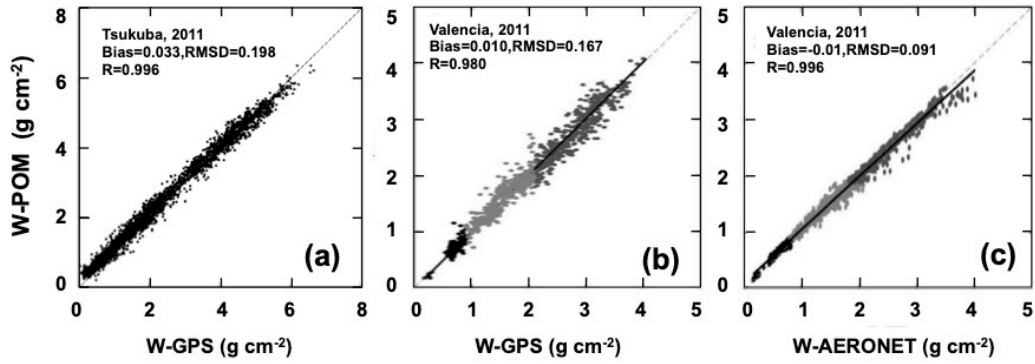
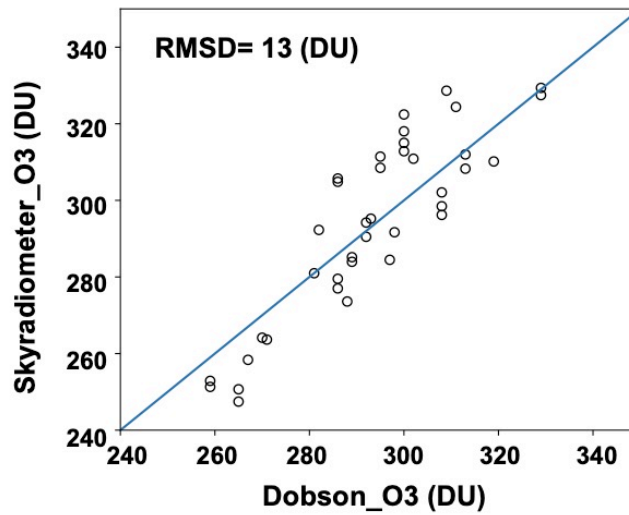


Fig. 11. Precipitable water retrieved by Uchiyama et al. (2014) in panel (a) and by Campanelli et al. (2018) in panels (b) and (c).



5

Fig. 12. Comparison of column ozone amount (DU) retrieved from the sky radiometer at MRI Tsukuba-site and from Dobson spectrometer at JMA Tateno Observatory from 13 December, 2012 to 8 January, 2013.

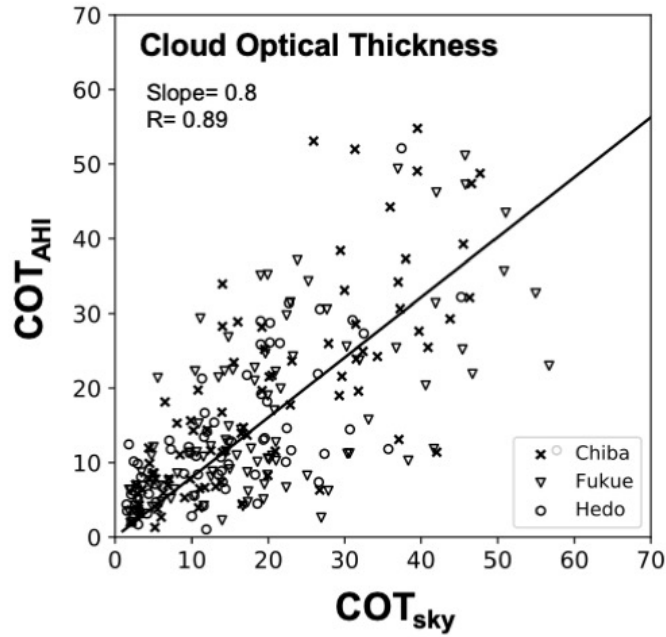


Fig. 13. Comparison of cloud optical thickness (COT) retrieved from sky radiometer at Chiba, Fukue and Hedo sites and Himawari-8/AHI satellite-borne imager in a period of October 2015 to December 2016 (Khatri et al., 2019). The regression line is with zero intercept constraint at the origin.

5

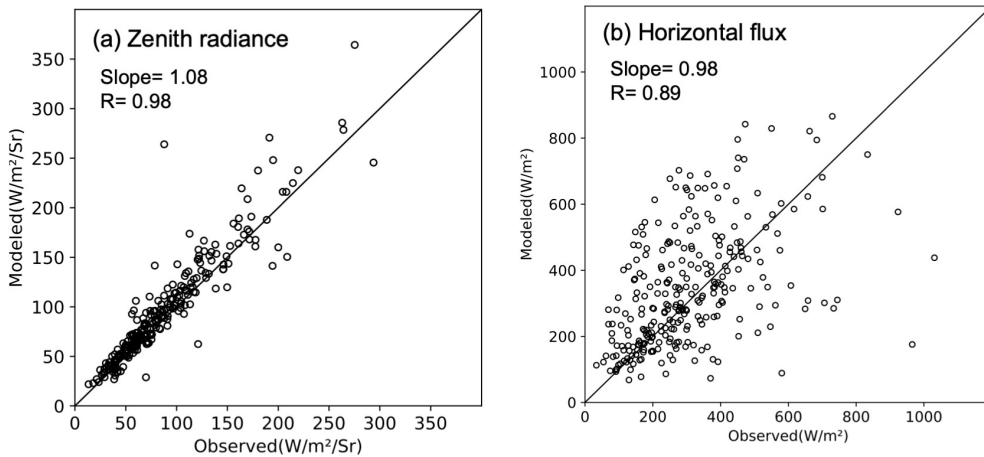


Fig. 14. Same as in Fig. 13 but for comparison between modeled and observed broad-band (a) radiances and (b) horizontal radiative fluxes. Regression lines are with zero intercept constraint at the origin.

10

End of manuscript